



Predicting the dynamics of thin-walled parts with curved surfaces in milling based on FEM and Taylor series

Dazhen Wang¹ · Junxue Ren¹ · Weijun Tian¹ · Kaining Shi¹ · Baogang Zhang¹

Received: 3 August 2018 / Accepted: 12 March 2019 / Published online: 27 March 2019
© Springer-Verlag London Ltd., part of Springer Nature 2019

Abstract

The effect of material removal on workpiece dynamics has a great influence on suppressing resonance and regenerative vibrations in milling of thin-walled structures. Although some works have been done to obtain the varying dynamics of the workpiece, many researchers take plate structures as research objects. In this paper, a method based on FEM and Taylor series is proposed to predict the time-varying dynamics of thin-walled blade structures in milling. The input data in the method is the mass and stiffness matrices of the initial workpiece and the change of the matrices caused by material removal. The initial matrices can be obtained through the FEM model established by the mechanical analysis of the eight-node shell element, and the change of the matrices can be obtained by a third-order Taylor series. In comparison with three-dimensional cube elements, the shell elements can reduce the number of degrees of freedom of the FEM model by 74%, which leads to about 9 times faster computation of the characteristic equation. Meanwhile, the proposed method eliminates the necessities of re-building and re-meshing the FEM model at each cutting position, then the computational efficiency of workpiece dynamics is improved. Finally, the result of experiments shows that the maximum prediction error of the proposed method is about 4%.

Keywords Thin-walled structure · Vibration · Time-varying dynamic parameter · FEM · Shell element · Taylor series

1 Introduction

Thin-walled parts have been widely used in aerospace industries such as blisk and engine blade. However, due to their characteristics of high flexibility, vibrations often occur during the semi-finishing and finishing stages of milling. This leads to poor surface quality and even can cause damage to the workpieces. Therefore, it is necessary to suppress the vibrations in machining process; what's more, the workpiece dynamics are the key to avoiding the vibrations.

In the past few decades, many researches have been done on machining vibrations. As a pioneer, Tobias [1] presented

that chatter results from the regeneration of chip thickness. To generate the stability lobes which contain chatter-free axial depth of cut and spindle rotation, many methods have been proposed. In the time domain, Smith and Tlustý [2] used the peak-to-peak diagrams to generate the stability lobes of milling. Insperger et al. [3] developed a semi-discretization (SD) method to calculate the stability lobes; then, Ding and Zhu et al. [4] expanded the SD method to a full discretization method and the calculation efficiency had been improved greatly. In addition, Bayly et al. [5] predicted the stability lobes by a temporal finite element analysis. In the frequency domain, Altintas and Budak [6] presented a single-frequency method to predict the stability lobes of milling. This method is efficient and fast, but it cannot be applicable to the milling with a low radial depth of cut. To overcome this problem, Merdol and Altintas [7] extended the method to a multi-frequency solution. To avoid chatter and predict the stable zone more precisely, Yan and Zhu [8] proposed an improved multi-frequency solution to predict the critical cutting depth in axial direction, and the dynamic properties of both milling tool and workpiece were considered. Comak and Budak [9] applied both semi-discretization and frequency domain methods to the stability

✉ Junxue Ren
rjx1968@nwpu.edu.cn

Dazhen Wang
wangdazhen@mail.nwpu.edu.cn

¹ The Key Laboratory of Contemporary Design and Integrated Manufacturing Technology, Ministry of Education, Northwestern Polytechnical University, Box 552, Xi'an, Shaanxi 710072, People's Republic of China



基于有限元和泰勒级数的曲面薄壁零件铣削动力学预测

王大震¹ – 任俊学¹ – 田卫军¹ – 史凯宁¹ – 张宝刚¹

收稿日期2018年8月3日 / 已接受：2019年3月12日 / 在线发表：2019年3月27日
© Springer-Verlag London Ltd., part of Springer Nature 2019

摘要

材料去除对工件动力学的影响对抑制薄壁结构铣削过程中的共振和再生振动有很大影响。虽然已经有一些研究获得了工件的动态变化，但很多研究者还是将板状结构作为研究对象。本文提出了一种基于有限元和泰勒级数的方法，用于预测薄壁叶片结构在铣削过程中的时变动力学。该方法的输入数据是初始工件的质量和刚度矩阵以及材料去除引起的矩阵变化。初始矩阵可通过八节点壳元素力学分析建立的有限元模型获得，矩阵的变化可通过三阶泰勒级数获得。与三维立方体元素相比，壳元素可将有限元模型的自由度数量减少74%，从而使特征方程的计算速度提高约9倍。同时，所提出的方法无需在每个切削位置重新建立有限元模型并重新网格化，从而提高了工件动力学的计算效率。最后，实验结果表明，所提方法的最大预测误差约为4%。

关键词 薄壁结构–振动–时变动态参数–有限元–壳元素–泰勒级数

1 引言

薄壁零件已广泛应用于航空航天领域，如叶盘和发动机叶片。然而，由于其具有高柔性的特点，在铣削的半精加工和精加工阶段经常会发生振动。这会导致表面质量变差，甚至会对工件造成损坏。因此，有必要抑制加工过程中的振动；而且，工件动力学是避免振动的关键。

在过去的几十年中，人们对加工振动进行了大量研究。作为先驱，Tobias [1] 提出了

任俊学 rjx1968@nwpu.edu.cn

王大震 wangdazhen@mail.nwpu.edu.cn

¹ 当代设计与集成制造技术教育部重点实验室、当代设计与集成制造技术教育部重点实验室、西北工业大学当代设计与集成制造技术教育部重点实验室，邮编552、中华人民共和国陕西省西安市 邮编：710072

振动是由切屑厚度再生引起的。为了产生包含无颤振轴向切削深度和主轴旋转的稳定叶，人们提出了许多方法。在时域中，Smith 和 Tlustý [2] 使用峰–峰图生成铣削稳定性裂片。Insperger 等人 [3] 开发了一种半离散化 (SD) 方法来计算稳定裂片；随后，Ding 和 Zhu 等人 [4] 将 SD 方法扩展为完全离散化方法，计算效率大大提高。此外，Bayly 等人 [5] 通过时域有限元分析预测了稳定裂片。在频域方面，Altintas 和 Budak [6] 提出了一种预测铣削稳定性裂片的单频方法。该方法高效、快速，但不适用于径向切深较小的铣削。为了克服这一问题，Merdol 和 Altintas [7] 将该方法扩展为多频率解决方案。为了避免颤振并更精确地预测稳定区域，Yan 和 Zhu [8] 提出了一种改进的多频方案来预测轴向临界切削深度，并考虑了铣刀和工件的动态特性。Comak 和 Budak [9] 采用半离散化和频域方法对稳定性进行了研究。

solution of variable geometry milling tools. Then, they developed a method for optimal selection of variable tool geometry to increase milling stability.

The above studies did not consider the effect of material removal on workpiece dynamics when stability lobes were established. However, material removal has a great influence on the dynamics of thin-walled parts in milling operations. In order to establish the stability lobes accurately, the influence of material removal on workpiece dynamics must be considered.

Some works have been done to consider the influence of material removal on workpiece dynamic behaviors. While Bravo and Altuzarra [10] used impact tests to obtain the dynamics of thin-walled parts at some milling steps; Seguy and Campa et al. [11] utilized FEM to study the evolutions of the dynamics of thin walls and a thin floor during milling. Thevenot and Arnaud et al. [12] used both experiments and a FEM model to study the change of workpiece dynamics in machining processes. Song and Ai et al. [13] used experimental data to adjust the results obtained by a FEM model. Then, the dynamic equations of the workpiece with time-variable dynamics were established. Filho and Negri et al. [14] obtained the changes of workpiece dynamic of a cantilever plate through a finite element model built by shell elements, then they predicted the stability lobe diagram for different tool positions.

To avoid frequently updating the FEM models and reduce the calculation time of workpiece dynamics, some methods have been proposed. Meshreki and Attia et al. [15] took into account the change of workpiece thickness and developed an analytical model to obtain the dynamics of thin-walled pockets during milling. Song and Liu et al. [16] used Sherman-Morrison-Woodbury formulas to estimate the frequency response functions (FRFs) of thin-walled parts in milling. Song and Shi et al. [17] proposed a comprehensive time-space discretization method to investigate the time-varying dynamic characteristics of thin-walled component milling process. Ahmadi [18] utilized finite strip models to get the workpiece dynamics of pocket structures in milling. Tuysuz and Altintas [19] presented an in-process model to update the dynamic behaviors of parts based on the full- and reduced-order dynamic substructuring in frequency domain.

However, the above studies are directed to plate structures. In [20], Yang and Zhang et al. took the thin-walled part with curved surfaces as an object of study, and they investigated the effect of variable dynamics on the stability in milling. Tuysuz and Altintas [21] presented an instantaneous modal parameter update model for the machined blade structures based on the reduced-order structural matrix decoupling and mode shape perturbation. And the proposed model was verified by cutting tests and the measured FRFs. Dang and Wan et al. [22] proposed a theoretical

method to predict the FRFs of the in-process workpiece by reducing the initial matrix dimensions and the in-analysis modes of the workpiece. And he studied the influences of tool position and material removal on the varying dynamic parameters during machining of straight plate and curved plate. Luo and Zhang et al. [23] employed a numerical simulation method to learn the dynamics evolution and machining stability of thin-walled blade structures in milling. Tian and Ren et al. [24] used a matrix perturbation method to calculate the natural frequencies of modified blade structures during milling. It can be seen that the studies [23, 24] simplified blade structures with curved surfaces into flat plate structures. However, while the mid-surface of flat plate structures is a plane, the mid-surface of blade structures is a curved surface. This makes the two structures have different mechanical properties. While the bending state and the thin film state in flat plate structures are not coupled to each other, the bending state and the thin film state of shell structures are coupled to each other and must be analyzed at the same time [25]. Therefore, the mechanical analysis of shell structures is much more complicated than that of flat plate structures.

In [26], Budak et al. obtained the initial FRFs of blade structures by a FEM model with 3D cube elements. Then, the elements were removed by the tool along the tool path and the workpiece dynamics were updated by the removed elements. On the one hand, the number of degrees of freedom (DOF) of the FEM model built by 3D cube elements is huge. On the other hand, it is time-consuming to update the FEM model of a machining process in a finite element analysis software. In this paper, a method is proposed to raise the efficiency of calculating the varying dynamics of blade structures by reducing the number of DOF of FEM models and avoiding re-building and re-meshing the FEM model frequently. The algorithm starts with obtaining the mass and stiffness matrices of the initial workpiece through the FEM model constructed by shell elements. Then, the initial mass and stiffness matrices are used to calculate the dynamics of the in-process workpiece by Taylor series. The accuracy and efficiency of the proposed method in obtaining workpiece dynamics are verified by comparing its performance against the FEM model built by 3D cube elements [26]. In addition, cutting and impact tests are performed on a thin-walled blade to verify the accuracy of the presented method.

The paper is organized as follows. In Section 2, the eight-node thick shell elements are used to model blade structures for obtaining the mass and stiffness matrices of the workpiece. In Section 3, a convergence analysis is performed to reduce the number of DOF of the FEM model. In Section 4, a third-order Taylor series is used to predict the workpiece dynamics in milling. In Section 5, the accuracy of the proposed method is verified by experiments.

可变几何铣削刀具的解决方案。然后，他们开发了一种优化选择可变刀具几何形状的方法，以提高铣削稳定性。

上述研究在建立稳定叶片时并未考虑材料去除对工件动力学的影响。然而，材料去除对铣削加工中薄壁零件的动力学有很大影响。为了准确建立稳定裂片，必须考虑材料去除对工件动力学的影响。

已有一些研究考虑了材料去除对工件动力学行为的影响。Bravo 和 Altuzarra [10] 利用冲击试验获得了薄壁零件在某些铣削步骤中的动力学特性；Seguy 和 Campa 等人 [11] 利用有限元研究了薄壁和薄底板在铣削过程中的动力学演变。Thevenot 和 Arnaud 等人 [12] 利用实验和有限元模型研究了加工过程中工件动力学的变化。Song 和 Ai 等人 [13] 利用实验数据调整有限元模型得出的结果。然后，建立了工件的时变动态方程。Filho 和 Negri 等人 [14] 通过壳元素建立的有限元模型获得了悬臂板的工件动态变化，然后预测了不同刀具位置下的稳定叶图。

为了避免频繁更新有限元模型并减少工件动力学计算时间，一些方法已被提出。Meshreki 和 Attia 等人 [15] 考虑了工件厚度的变化，建立了一个分析模型来获得薄壁口袋在铣削过程中的动力学特性。Song 和 Liu 等人 [16] 使用 Sherman-Morrison-Woodbury 公式估算了铣削过程中薄壁零件的频率响应函数 (FRF)。Song 和 Shi 等人 [17] 提出了一种综合时空离散方法来研究薄壁零件铣削过程的时变动态特性。Ahmadi [18] 利用有限条带模型获得了铣削过程中袋状结构的工件动力学特性。Tuysuz 和 Altintas [19] 基于频域中的全阶和降阶动态子结构，提出了一种更新零件动态行为的过程中模型。

然而，上述研究均针对板状结构。在 [20] 中，Yang 和 Zhang 等人以曲面薄壁零件为研究对象，研究了变量动力学对铣削稳定性的影响。Tuysuz 和 Altintas [21] 基于降阶结构矩阵解耦和模态振型扰动，提出了加工叶片结构的瞬时模态参数更新模型。并通过切削试验和测量的 FRF 验证了所提出的模型。Dang 和 Wan 等人 [22] 提出了一种理论上的叶片结构改进模型。

他提出了一种通过减少初始矩阵尺寸和工件的分析模型来预测加工中工件 FRF 的方法。他还研究了直板和曲面板加工过程中刀具位置和材料去除率对不同动态参数的影响。Luo和Zhang等人[23]采用数值模拟方法研究了薄壁叶片结构在铣削加工中的动力学演变和加工稳定性。Tian和Ren等[24]采用矩阵扰动法计算了铣削过程中改性叶片结构的固有频率。可以看出，[23, 24] 的研究将曲面叶片结构简化为平板结构。然而，平板结构的中表面是一个平面，而叶片结构的中表面是一个曲面。这使得两种结构具有不同的力学性能。平板结构的弯曲状态和薄膜状态并不相互耦合，而壳体结构的弯曲状态和薄膜状态相互耦合，必须同时进行分析 [25]。因此，壳体结构的力学分析比平板结构复杂得多。

在 [26] 中，Budak 等人通过三维立方体元素有限元模型获得了叶片结构的初始 FRF。然后，刀具沿刀具路径移除元素，并通过移除的元素更新工件动力学。一方面，由三维立方体元素建立的有限元模型自由度 (DOF) 数量巨大。另一方面，在有限元分析软件中更新加工过程的有限元模型非常耗时。本文提出了一种方法，通过减少有限元模型的 DOF 数，避免频繁地重新建立和重新网格化有限元模型，从而提高叶片结构变化动力学计算的效率。该算法首先通过壳元素构建的有限元模型获得初始工件的质量和刚度矩阵。然后，利用初始质量和刚度矩阵通过泰勒级数计算加工中工件的动力学。通过与由三维立方体元素构建的有限元模型进行比较，验证了所提方法在获取工件动力学方面的准确性和效率 [26]。此外，还对薄壁叶片进行了切割和冲击试验，以验证所提方法的准确性。

本文的结构安排如下。第 2 节，使用八节点厚壳元素建立叶片结构模型，以获得工件的质量和刚度矩阵。第 3 节，进行收敛分析以减少有限元模型的 DOF 数。第 4 节，使用三阶泰勒级数预测铣削过程中的工件动态。第 5 节通过实验验证了所提方法的准确性。

2 FEM model of blade structures built by shell elements

The motion equation of free vibrations of blade structures can be written as:

$$\mathbf{M}\ddot{\mathbf{x}} + \mathbf{C}\dot{\mathbf{x}} + \mathbf{K}\mathbf{x} = \mathbf{0} \quad (1)$$

where \mathbf{x} , $\dot{\mathbf{x}}$, and $\ddot{\mathbf{x}}$ are displacement, velocity, and acceleration vectors. \mathbf{M} , \mathbf{C} , and \mathbf{K} are mass, damping, and stiffness matrices of the workpiece. When the damping is ignored, the above equation can be simplified as:

$$\mathbf{M}\ddot{\mathbf{x}} + \mathbf{K}\mathbf{x} = \mathbf{0} \quad (2)$$

The characteristic equation of Eq. 2 can be written as:

$$(\mathbf{K} - \lambda\mathbf{M})\mathbf{Q} = \mathbf{0} \quad (3)$$

where λ and \mathbf{Q} represent the eigenvalues and the eigenvectors. The natural frequencies ω and the corresponding mode shapes can be written as $\sqrt{\lambda}$ and \mathbf{Q} , respectively. So, for calculating the dynamics of blade structures, the mass and stiffness matrices of the workpiece must be obtained. In this paper, the matrices are obtained by FEM. Although 3D cube elements are simpler than shell elements, the eight-node thick shell element [25] with 40 DOF shown in Fig. 1 is used to model the blade structure for reducing the number of DOF of the model on the premise of ensuring the accuracy of calculation. Where $s-t-n$ represents a natural coordinate system, the range of s , t , and n is $[-1, 1]$.

2.1 Geometric parameters of the blade structure

When the shell elements are used to model the blade, the workpiece thickness, the coordinates of the point on the blade mid-surface, and the corresponding normal vector of the mid-surface should be obtained first.

The cross section of blade structures can be simplified to two curves as shown in Fig. 2. Since the x -coordinates of

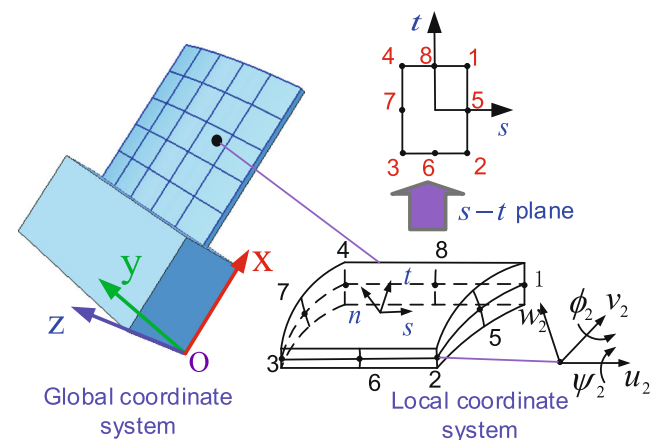


Fig. 1 Eight-node thick shell element

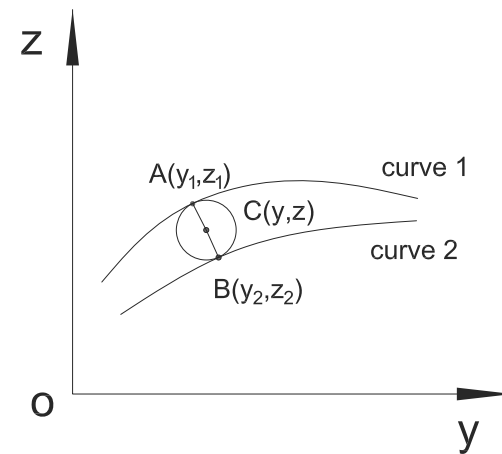


Fig. 2 Cross section of blade structures

the points on the cross section are equal, the x -coordinate is ignored. Suppose that $C(y, z)$ is a point on the mid-surface, then the point C is taken as the center and a circle simultaneously tangent to curve 1 at $A(y_1, z_1)$ and tangent to curve 2 at $B(y_2, z_2)$ is constructed, then the radius of the circle can be expressed as:

$$R = \sqrt{(y - y_1)^2 + (z - z_1)^2} = \sqrt{(y - y_2)^2 + (z - z_2)^2} \quad (4)$$

Assuming the equation of curve 1 is $z_1 = f_1(y_1)$, the equation of curve 2 is $z_2 = f_2(y_2)$. Since the circle is tangent to curves 1 and 2, we can obtain:

$$\begin{cases} f_1' \frac{z - z_1}{y - y_1} = -1 \\ f_2' \frac{z - z_2}{y - y_2} = -1 \end{cases} \quad (5)$$

where f_1' represents the derivative of $z_1 = f_1(y_1)$ with respect to y_1 , which is the slope of curve 1 at point $A(y_1, z_1)$; f_2' represents the derivative of $z_2 = f_2(y_2)$ with respect to y_2 , which is the slope of curve 2 at point $B(y_2, z_2)$. From Eqs. 4 and 5, we can obtain:

$$[(y_1 - y_2)^2 - (z_1 - z_2)^2](f_1' + f_2') + 2(y_1 - y_2)(z_1 - z_2)(f_1'f_2' - 1) = 0 \quad (6)$$

The above equation can be expressed as a function of y_2 :

$$g(y_2) = [(y_1 - y_2)^2 - (z_1 - z_2)^2](f_1' + f_2') + 2(y_1 - y_2)(z_1 - z_2)(f_1'f_2' - 1) \quad (7)$$

Expressing curves 1 and 2 as the parametric functions of u_1 and u_2 :

$$\begin{cases} y_1 = y_1(u_1) \\ z_1 = z_1(u_1) \end{cases}; \begin{cases} y_2 = y_2(u_2) \\ z_2 = z_2(u_2) \end{cases}; (u_1, u_2 \in [0, 1]) \quad (8)$$

2 由壳元素构建的叶片结构有限元模型

叶片结构自由振动的运动方程可写成

(1) 式中 \mathbf{x} , $\dot{\mathbf{x}}$, 和 $\ddot{\mathbf{x}}$ 分别为位移矢量、速度矢量和加速度矢量。 \mathbf{M} 、 \mathbf{C} 和 \mathbf{K} 是工件的质量矩阵、阻尼矩阵和刚度矩阵。当忽略阻尼时，上式可简化为

$$\mathbf{M}\ddot{\mathbf{x}} + \mathbf{K}\mathbf{x} = \mathbf{0} \quad (2)$$

公式 2 的特征方程可写成

(3) 其中， λ 和 \mathbf{Q} 分别代表特征值和特征向量。固有频率 ω 和相应的模态振型可分别写成 $\sqrt{\lambda}$ 和 \mathbf{Q} 。因此，要计算叶片结构的动力学特性，必须获得工件的质量矩阵和刚度矩阵。在本文中，这些矩阵是通过有限元求得的。虽然三维立方体元素比壳元素简单，但为了保证计算精度的前提下减少模型的 DOF 数，本文采用图 1 所示的具有 40 个 DOF 的八节点厚壳元素 [25] 来建立叶片结构模型。其中， $s-t-n$ 表示自然坐标系， s 、 t 和 n 的取值范围为 $[-1, 1]$ 。

2.1 叶片结构的几何参数

使用壳元素建立叶片模型时，应首先获得工件厚度、叶片中面上点的坐标以及相应的中面法向矢量。

叶片结构的横截面可简化为两条曲线，如图 2 所示。由于叶片结构的 x 坐标为

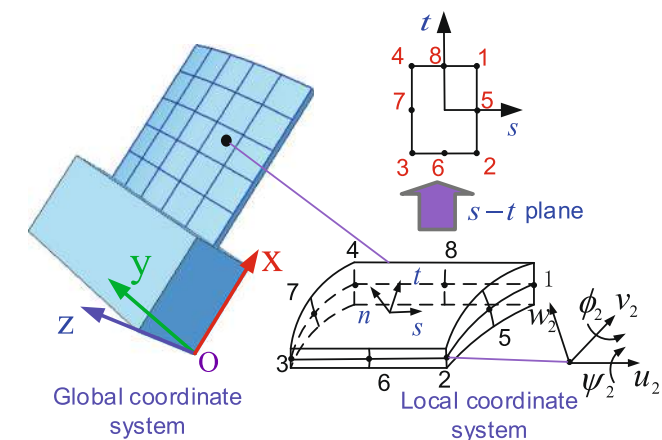


图 1 八节点厚壳元素

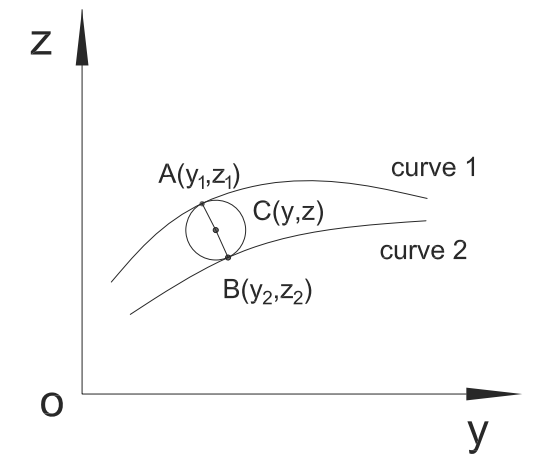


图 2 叶片结构的横截面

如果横截面上的各点相等，则忽略 x 坐标。假设 $C(y, z)$ 是中面上的一点，则以 C 点为圆心，同时在 $A(y_1, z_1)$ 处与曲线 1 相切，在 $B(y_2, z_2)$ 处与曲线 2 相切，则圆的半径可表示为：

$$R = \sqrt{(y - y_1)^2 + (z - z_1)^2} = \sqrt{(y - y_2)^2 + (z - z_2)^2} \quad (4)$$

假设曲线 1 的方程为 $z_1 = f_1(y_1)$ ，则曲线 2 的方程为 $z_2 = f_2(y_2)$ 。由于圆与曲线 1 和 2 相切，我们可以得到

$$\begin{cases} f_1' \frac{z - z_1}{y - y_1} = -1 \\ f_2' \frac{z - z_2}{y - y_2} = -1 \end{cases} \quad (5)$$

其中， f_1' 表示 $z_1 = f_1(y_1)$ 相对于 y_1 的导数，即曲线 1 在 A 点 (y_1, z_1) 的斜率； f_2' 表示 $z_2 = f_2(y_2)$ 相对于 y_2 的导数，即曲线 2 在 B 点 (y_2, z_2) 的斜率。根据公式 4 和 5，我们可以得到

$$[(y_1 - y_2)^2 - (z_1 - z_2)^2](f_1' + f_2') + 2(y_1 - y_2)(z_1 - z_2)(f_1'f_2' - 1) = 0 \quad (6)$$

上式可表示为 y_2 的函数：

$$g(y_2) = [(y_1 - y_2)^2 - (z_1 - z_2)^2](f_1' + f_2') + 2(y_1 - y_2)(z_1 - z_2)(f_1'f_2' - 1) \quad (7)$$

将曲线 1 和 2 表示为 u_1 和 u_2 的参数函数：

$$\begin{cases} y_1 = y_1(u_1) \\ z_1 = z_1(u_1) \end{cases}; \begin{cases} y_2 = y_2(u_2) \\ z_2 = z_2(u_2) \end{cases}; (u_1, u_2 \in [0, 1]) \quad (8)$$

Then, Eq. 7 can be expressed as a function of u_2 :

$$g(u_2) = [(y_1 - y_2(u_2))^2 - (z_1 - z_2(u_2))^2](f'_1 + f'_2(u_2)) + 2(y_1 - y_2(u_2))(z_1 - z_2(u_2))(f'_1 f'_2(u_2) - 1) \quad (9)$$

The first derivative of $g(u_2)$ with respect to u_2 can be expressed as:

$$g'_{u_2} = [-2(y_1 - y_2)y'_{2u_2} + 2(z_1 - z_2)z'_{2u_2}](f'_1 + f'_2) + [(y_1 - y_2)^2 - (z_1 - z_2)^2 + 2(y_1 - y_2)(z_1 - z_2)f'_1]y'_{2u_2}f''_2 - 2(f'_1 f'_2 - 1)[y'_{2u_2}(z_1 - z_2) + (y_1 - y_2)z'_{2u_2}] \quad (10)$$

where y'_{2u_2} and z'_{2u_2} represent the first partial derivatives of y_2 and z_2 with respect to u_2 , respectively. Meanwhile, f''_2 represents the second partial derivative of $z_2 = f_2(y_2)$ with respect to y_2 . According to Eq. 8, f'_1 , f'_2 , and f''_2 can be expressed as:

$$\begin{cases} f'_1 = \frac{\partial z_1}{\partial u_1} \frac{\partial u_1}{\partial y_1} = \frac{z'_{1u_1}}{y'_{1u_1}} \\ f'_2 = \frac{\partial z_2}{\partial u_2} \frac{\partial u_2}{\partial y_2} = \frac{z'_{2u_2}}{y'_{2u_2}} \\ f''_2 = \frac{y'_{2u_2} z''_{2u_2} - z'_{2u_2} y''_{2u_2}}{(y'_{2u_2})^3} \end{cases} \quad (11)$$

where y'_{1u_1} and z'_{1u_1} represent the first partial derivatives of y_1 and z_1 with respect to u_1 ; y''_{2u_2} and z''_{2u_2} represent the second partial derivatives of y_2 and z_2 with respect to u_2 .

Assuming the point (y_1, z_1) on curve 1 is known, then the corresponding point (y_2, z_2) on curve 2 can be obtained as follows:

- step 1 Importing the parameters of cross sections from the file in IGES format into Matlab by the function *iges2matlab*;
- step 2 Inserting n points in curve 1 with the type of equal parameters, each point corresponds with a u_1 and $u_1 \in [0, 1]$;
- step 3 For each u_1 , the function *nrbevalIGES* is used to obtain y_1, z_1, y'_{1u_1} and z'_{1u_1} ;
- step 4 Using the Newton iteration method to calculate u_2 :
 - (a) Giving initial value $u_{2,1} = u_0$ and allowance error e of the root of equation $g(u_2) = 0$;
 - (b) For $u_{2,k}$ ($k = 1, 2, \dots$), *nrbevalIGES* is used to obtain $y_{2,k}, z_{2,k}, y'_{2u_2,k}, z'_{2u_2,k}, y''_{2u_2,k}$ and $z''_{2u_2,k}$;
 - (c) $g(u_{2,k})$ is calculated by Eq. 9, if $|g(u_{2,k})| \leq e$, then $u_2 = u_{2,k}$, $y_2 = y_{2,k}$, $z_2 = z_{2,k}$, $y'_{2u_2} = y'_{2u_2,k}$, $z'_{2u_2} = z'_{2u_2,k}$, if the condition is not satisfied, go to step (4d);
 - (d) $g'(u_{2,k})$ is obtained by Eq. 10, then $u_{2,k+1} = u_{2,k} - \frac{g(u_{2,k})}{g'(u_{2,k})}$; go to step (4b).

When $(y_1, z_1), y'_{1u_1}, z'_{1u_1}, (y_2, z_2), y'_{2u_2}, z'_{2u_2}$ correspond with u_1 and u_2 have been obtained. The coordinates (y, z) of point C can be obtained by Eq. 5. Meanwhile, the diameter of the circle obtained by Eq. 4 is regarded as the workpiece thickness at point C . Then, the coordinates of the points on the mid-surface are imported into NX 9.0, the middle curves and the mid-surface of the blade can be obtained by fitting. The procedure for obtaining the mid-surface of a blade is shown in Fig. 3. After the mid-surface has been obtained, the function *UF_MODAL_ask_face_props* of UG/Open is used to obtain the normal vectors of the mid-surface. The coordinates (x_i, y_i, z_i) of point i on the mid-surface, the workpiece thickness at point i , and the corresponding normal vector $\mathbf{m}_i = (\mathbf{H}_{3i}(1), \mathbf{H}_{3i}(2), \mathbf{H}_{3i}(3))$ of the mid-surface are the key data to establish the FEM model of the blade.

2.2 Mass and stiffness matrices

The aim of establishing the FEM model of blade structures is to obtain the mass and stiffness matrices of the workpiece, then the workpiece dynamics can be calculated by the matrices. The mass and stiffness matrices can be obtained as follows.

Geometric description of the shell element The global coordinates of any point in the shell element can be expressed as:

$$\begin{Bmatrix} x \\ y \\ z \end{Bmatrix} = \sum_{i=1}^8 N_i \begin{Bmatrix} x_i \\ y_i \\ z_i \end{Bmatrix}_{MID} + \sum_{i=1}^8 N_i \frac{n}{2} \begin{Bmatrix} \mathbf{H}_{3i}(1)t_i \\ \mathbf{H}_{3i}(2)t_i \\ \mathbf{H}_{3i}(3)t_i \end{Bmatrix} \quad (12)$$

where N_i are the shape functions, *MID* represents the mid-surface of the shell, (x_i, y_i, z_i) are the coordinates of node i on the shell mid-surface, $\mathbf{H}_{3i}(1), \mathbf{H}_{3i}(2)$, and $\mathbf{H}_{3i}(3)$ are the components of the normal vector \mathbf{m}_i of the mid-surface, and t_i is the shell thickness. For the node numbering as shown in Fig. 1, the shape functions can be written as:

$$\begin{cases} N_1 = \frac{1}{4}(1+s)(1+t)(s+t-1) \\ N_2 = \frac{1}{4}(1+s)(1-t)(s-t-1) \\ N_3 = \frac{1}{4}(1-s)(1-t)(-s-t-1) \\ N_4 = \frac{1}{4}(1-s)(1+t)(-s+t-1) \\ N_5 = \frac{1}{2}(1+s)(1-t^2), N_6 = \frac{1}{2}(1-s^2)(1-t) \\ N_7 = \frac{1}{2}(1-s)(1-t^2), N_8 = \frac{1}{2}(1-s^2)(1+t) \end{cases} \quad (13)$$

Defining the matrix N There are three linear displacements and two angular displacements of node i . Three orthogonal vectors $\mathbf{H}_{1i}, \mathbf{H}_{2i}$, and \mathbf{H}_{3i} are constructed to define the

那么, 式 7 可以表示为 u_2 :

$$g(u_2) = [(y_1 - y_2(u_2))^2 - (z_1 - z_2(u_2))^2](f'_1 + f'_2(u_2)) + 2(y_1 - y_2(u_2))(z_1 - z_2(u_2))(f'_1 f'_2(u_2) - 1) \quad (9)$$

(9) $g(u_2)$ 关于 u_2 的一阶导数可表示为

$$g'_{u_2} = [-2(y_1 - y_2)y'_{2u_2} + 2(z_1 - z_2)z'_{2u_2}](f'_1 + f'_2) + [(y_1 - y_2)^2 - (z_1 - z_2)^2 + 2(y_1 - y_2)(z_1 - z_2)f'_1]y'_{2u_2}f''_2 - 2(f'_1 f'_2 - 1)[y'_{2u_2}(z_1 - z_2) + (y_1 - y_2)z'_{2u_2}] \quad (10)$$

其中 y'_{2u_2} 和 z'_{2u_2} 分别表示 y_2 和 z_2 相对于 u_2 的第一次偏导数。同时, f''_2 表示 $z_2 = f_2(y_2)$ 相对于 y_2 的二次偏导数。根据公式 8, f'_1 、 f'_2 和 f''_2 可表示为

$$\begin{cases} f'_1 = \frac{\partial z_1}{\partial u_1} \frac{\partial u_1}{\partial y_1} = \frac{z'_{1u_1}}{y'_{1u_1}} \\ f'_2 = \frac{\partial z_2}{\partial u_2} \frac{\partial u_2}{\partial y_2} = \frac{z'_{2u_2}}{y'_{2u_2}} \\ f''_2 = \frac{y'_{2u_2} z''_{2u_2} - z'_{2u_2} y''_{2u_2}}{(y'_{2u_2})^3} \end{cases} \quad (11)$$

其中 y'_{1u_1} 和 z'_{1u_1} 表示 y_1 和 z_1 相对于 u_1 的第一偏导数; y''_{2u_2} 和 z''_{2u_2} 表示 y_2 和 z_2 相对于 u_2 的第二偏导数。

假设曲线 1 上的点 (y_1, z_1) 已知, 则曲线 2 上的相应点 (y_2, z_2) 可按下式求得:

步骤 1 使用函数 *iges2matlab* 将 IGES 格式文件中的横截面参数导入 Matlab;

步骤 2 在曲线 1 中插入 n 个参数相等的点, 每个点分别对应一个 u_1 和 $u_1 \in [0, 1]$;

步骤 3 对于每个 u_1 , 使用函数 *nrbevalIGES* 得到 y_1, z_1, y'_{1u_1} 和 z'_{1u_1} ; 步骤 4 使用牛顿迭代法计算 u_2 :

- (a) 给出初始值 $u_{2,1} = u_0$ 和方程 $g(u_2) = 0$ 的根的余量误差 e ;
- (b) 对于 $u_{2,k}$ ($k = 1, 2, \dots$), 使用 *nrbevalIGES* 求得 $y_{2,k}, z_{2,k}, y'_{2u_2,k}, z'_{2u_2,k}, y''_{2u_2,k}$ 和 $z''_{2u_2,k}$;
- (c) $g(u_{2,k})$ 由式 9 计算, 若 $|g(u_{2,k})| \leq e$, 则 $u_2 = u_{2,k}$, $y_2 = y_{2,k}$, $z_2 = z_{2,k}$, $y'_{2u_2} = y'_{2u_2,k}$, $z'_{2u_2} = z'_{2u_2,k}$, 若不满足条件, 转至步骤 (4d);
- (d) $g'(u_{2,k})$ 由公式 10 得出, 则 $u_{2,k+1} = u_{2,k} - \frac{g(u_{2,k})}{g'(u_{2,k})}$; 转至步骤 (4b)。

当 $(y_1, z_1), y'_{1u_1}, z'_{1u_1}, (y_2, z_2), y'_{2u_2}, z'_{2u_2}$ 与 u_1 和 u_2 相对应时已经得到。点 C 的坐标 (y, z) 可由公式 5 得出。同时, 将公式 4 得出的圆直径视为 C 点的工件厚度。然后, 将中面上各点的坐标导入 NX 9.0, 通过拟合即可得到叶片的中间曲线和中面。获取叶片中面的过程如图 3 所示。获得中面后, 使用 UG/Open 的 *UF_MODAL_ask_face_props* 函数获得中面的法向量。中面上第 i 点的坐标 (x_i, y_i, z_i) 、第 i 点的工件厚度以及相应的中面法向矢量 $\mathbf{m}_i = (\mathbf{H}_{3i}(1), \mathbf{H}_{3i}(2), \mathbf{H}_{3i}(3))$ 是建立叶片有限元模型的关键数据。

2.2 质量和刚度矩阵

建立叶片结构有限元模型的目的是获得工件的质量和刚度矩阵, 然后通过矩阵计算工件的动力学特性。质量矩阵和刚度矩阵的计算公式如下。

壳元素的几何描述 壳元素中任意点的全局坐标可表示为

$$\begin{Bmatrix} x \\ y \\ z \end{Bmatrix} = \sum_{i=1}^8 N_i \begin{Bmatrix} x_i \\ y_i \\ z_i \end{Bmatrix}_{MID} + \sum_{i=1}^8 N_i \frac{n}{2} \begin{Bmatrix} \mathbf{H}_{3i}(1)t_i \\ \mathbf{H}_{3i}(2)t_i \\ \mathbf{H}_{3i}(3)t_i \end{Bmatrix} \quad (12)$$

其中 N_i 是形状函数, *MID* 代表壳的中表面, (x_i, y_i, z_i) 是节点 i 在壳中表面上的坐标, $\mathbf{H}_{3i}(1), \mathbf{H}_{3i}(2), \mathbf{H}_{3i}(3)$ 是中表面法向量 \mathbf{m}_i 的分量, t_i 是壳的厚度。对于如图 1 所示的节点编号, 形状函数可以写为

$$\begin{cases} N_1 = \frac{1}{4}(1+s)(1+t)(s+t-1) \\ N_2 = \frac{1}{4}(1+s)(1-t)(s-t-1) \\ N_3 = \frac{1}{4}(1-s)(1-t)(-s-t-1) \\ N_4 = \frac{1}{4}(1-s)(1+t)(-s+t-1) \\ N_5 = \frac{1}{2}(1+s)(1-t^2), N_6 = \frac{1}{2}(1-s^2)(1-t) \\ N_7 = \frac{1}{2}(1-s)(1-t^2), N_8 = \frac{1}{2}(1-s^2)(1+t) \end{cases} \quad (13)$$

定义矩阵 N 节点 i 有三个线性位移和两个角位移。构建三个正交矢量 $\mathbf{H}_{1i}, \mathbf{H}_{2i}$ 和 \mathbf{H}_{3i} , 以定义

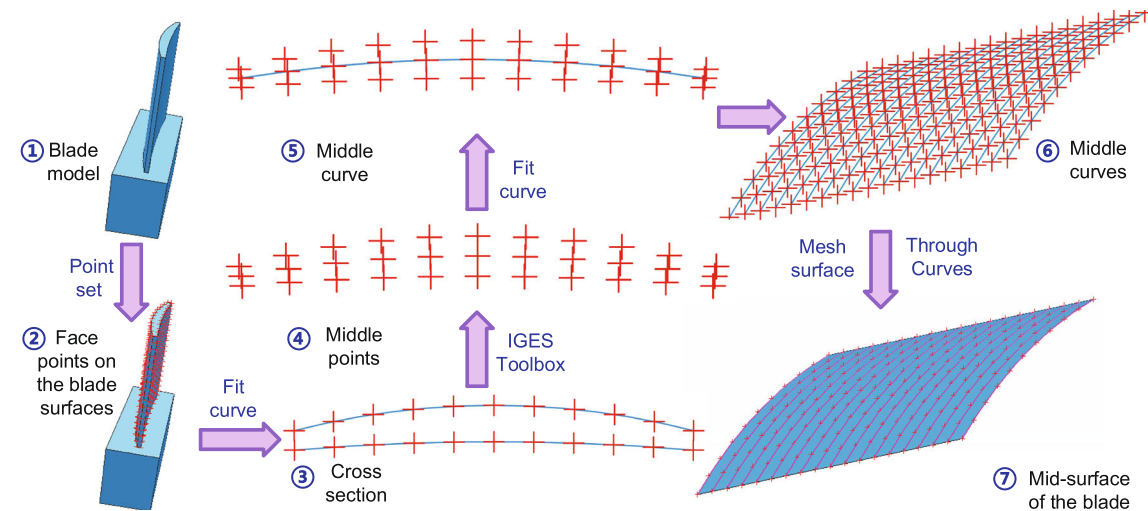


Fig. 3 Procedure for obtaining the mid-surface of a blade

angular displacements of node i . Here, \mathbf{H}_{3i} is a vector in the normal direction of the mid-surface at point i . \mathbf{H}_{2i} and \mathbf{H}_{1i} are two vectors which are tangent to the mid-surface and orthogonal to the vector \mathbf{H}_{3i} that can be constructed as:

$$\mathbf{H}_{2i} = \mathbf{H}_{3i} \times \mathbf{i} (\text{the } x\text{-axis}), \quad \mathbf{H}_{1i} = \mathbf{H}_{2i} \times \mathbf{H}_{3i} \quad (14)$$

When the vectors have been constructed, the direction cosines l_{1i}, m_{1i}, n_{1i} of \mathbf{H}_{1i} and the direction cosines l_{2i}, m_{2i}, n_{2i} of \mathbf{H}_{2i} can be obtained. The direction cosines of \mathbf{H}_{3i} are $l_{3i} = \mathbf{H}_{3i}(1)$, $m_{3i} = \mathbf{H}_{3i}(2)$, and $n_{3i} = \mathbf{H}_{3i}(3)$. Then, the displacements of any point in the element can be obtained by the node displacements $\delta_i = [u_i, v_i, w_i, \phi_i, \psi_i]^T$ and the shape functions $N_i(s, t)$, as follows:

$$\begin{Bmatrix} u \\ v \\ w \end{Bmatrix} = \sum_{i=1}^8 N_i \begin{Bmatrix} u_i \\ v_i \\ w_i \end{Bmatrix} + \sum_{i=1}^8 \frac{n N_i t_i}{2} \begin{Bmatrix} l_{1i} & l_{2i} \\ m_{1i} & m_{2i} \\ n_{1i} & n_{2i} \end{Bmatrix} \begin{Bmatrix} \phi_i \\ \psi_i \end{Bmatrix} \quad (15)$$

Then, the matrix \mathbf{N} is defined by Eq. 15 as:

$$\mathbf{N} = \begin{bmatrix} N_1 & 0 & 0 & \frac{n N_1 t_1}{2} l_{11} & \frac{n N_1 t_1}{2} l_{21} & \cdots \\ 0 & N_1 & 0 & \frac{n N_1 t_1}{2} m_{11} & \frac{n N_1 t_1}{2} m_{21} & \cdots \\ 0 & 0 & N_1 & \frac{n N_1 t_1}{2} n_{11} & \frac{n N_1 t_1}{2} n_{21} & \cdots \\ N_8 & 0 & 0 & \frac{n N_8 t_8}{2} l_{18} & \frac{n N_8 t_8}{2} l_{28} & \cdots \\ 0 & N_8 & 0 & \frac{n N_8 t_8}{2} m_{18} & \frac{n N_8 t_8}{2} m_{28} & \cdots \\ 0 & 0 & N_8 & \frac{n N_8 t_8}{2} n_{18} & \frac{n N_8 t_8}{2} n_{28} & \cdots \end{bmatrix} \quad (16)$$

Defining the geometric matrix \mathbf{B} In order to obtain the strain of shell elements in local coordinate systems, the local

coordinate system $\mathbf{x}' - \mathbf{y}' - \mathbf{z}'$ should be constructed. The \mathbf{z}' axis can be constructed as:

$$\mathbf{z}' = N_1 \mathbf{H}_{31} + N_2 \mathbf{H}_{32} + \cdots + N_8 \mathbf{H}_{38} \quad (17)$$

After, the direction cosines l_3, m_3, n_3 of \mathbf{z}' can be obtained. Then, \mathbf{y}' and \mathbf{x}' can be constructed as:

$$\mathbf{y}' = \mathbf{z}' \times \mathbf{x} = \begin{bmatrix} i & j & k \\ l_3 & m_3 & n_3 \\ 1 & 0 & 0 \end{bmatrix}, \quad \mathbf{x}' = \mathbf{z}' \times \mathbf{y}' \quad (18)$$

The direction cosines l_2, m_2, n_2 of \mathbf{y}' and the direction cosines l_1, m_1, n_1 of \mathbf{x}' can be obtained. Then, the direction cosine matrix of the local coordinate system $\mathbf{x}' - \mathbf{y}' - \mathbf{z}'$ can be expressed as:

$$\mathbf{DCM} = \begin{bmatrix} l_1 & l_2 & l_3 \\ m_1 & m_2 & m_3 \\ n_1 & n_2 & n_3 \end{bmatrix} \quad (19)$$

The matrix \mathbf{DCM} is used to transform the derivatives of displacements u, v , and w to the derivatives of local displacements u', v' , and w' .

$$\begin{bmatrix} \frac{\partial u'}{\partial x'} & \frac{\partial v'}{\partial x'} & \frac{\partial w'}{\partial x'} \\ \frac{\partial u'}{\partial y'} & \frac{\partial v'}{\partial y'} & \frac{\partial w'}{\partial y'} \\ \frac{\partial u'}{\partial z'} & \frac{\partial v'}{\partial z'} & \frac{\partial w'}{\partial z'} \end{bmatrix} = \mathbf{DCM}^T \begin{bmatrix} \frac{\partial u}{\partial x} & \frac{\partial v}{\partial x} & \frac{\partial w}{\partial x} \\ \frac{\partial u}{\partial y} & \frac{\partial v}{\partial y} & \frac{\partial w}{\partial y} \\ \frac{\partial u}{\partial z} & \frac{\partial v}{\partial z} & \frac{\partial w}{\partial z} \end{bmatrix} \mathbf{DCM} \quad (20)$$

where:

$$\begin{bmatrix} \frac{\partial u}{\partial x} & \frac{\partial v}{\partial x} & \frac{\partial w}{\partial x} \\ \frac{\partial u}{\partial y} & \frac{\partial v}{\partial y} & \frac{\partial w}{\partial y} \\ \frac{\partial u}{\partial z} & \frac{\partial v}{\partial z} & \frac{\partial w}{\partial z} \end{bmatrix} = \mathbf{J}^{-1} \begin{bmatrix} \frac{\partial u}{\partial s} & \frac{\partial v}{\partial s} & \frac{\partial w}{\partial s} \\ \frac{\partial u}{\partial t} & \frac{\partial v}{\partial t} & \frac{\partial w}{\partial t} \\ \frac{\partial u}{\partial n} & \frac{\partial v}{\partial n} & \frac{\partial w}{\partial n} \end{bmatrix} \quad (21)$$

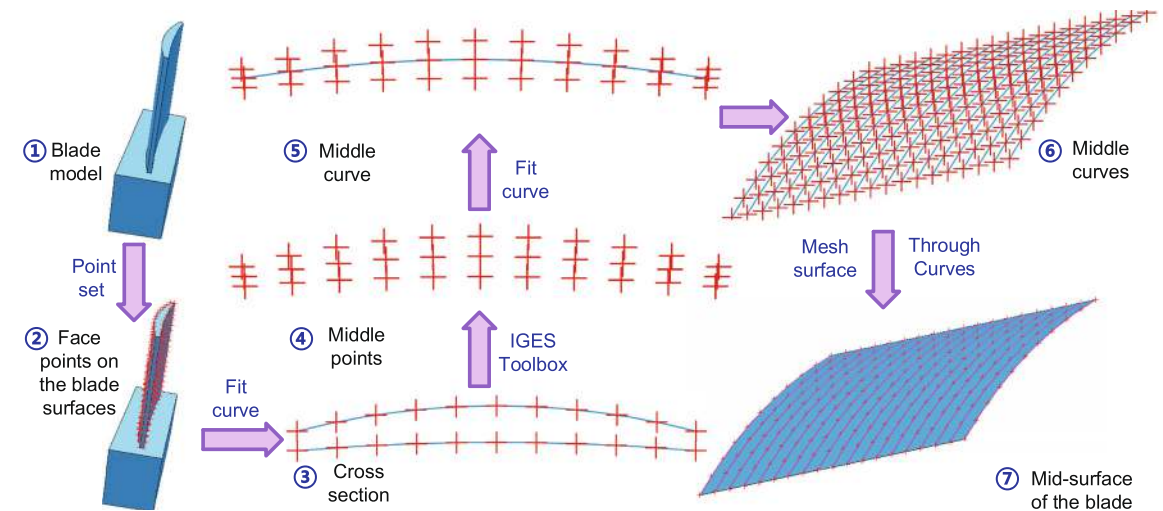


图 3 获取叶片中表面的步骤

节点 i 的角位移。这里, \mathbf{H}_{3i} 是第 i 点中表面法线方向上的矢量。 \mathbf{H}_{2i} 和 \mathbf{H}_{1i} 是两个矢量, 它们与中表面相切, 并与矢量 \mathbf{H}_{3i} 正交, 可构造为: \mathbf{H}_{2i} 和 \mathbf{H}_{1i} 的角位移:

$$\mathbf{H}_{2i} = \mathbf{H}_{3i} \times \mathbf{i} (\text{x 轴}), \quad \mathbf{H}_{1i} = \mathbf{H}_{2i} \times \mathbf{H}_{3i} \quad (14)$$

矢量建好后, 就可以得到 \mathbf{H}_{1i} 的方向余弦 l_{1i}, m_{1i}, n_{1i} 和 \mathbf{H}_{2i} 的方向余弦 l_{2i}, m_{2i}, n_{2i} 。 \mathbf{H}_{3i} 的方向余弦为 $l_{3i} = \mathbf{H}_{3i}(1)$, $m_{3i} = \mathbf{H}_{3i}(2)$, $n_{3i} = \mathbf{H}_{3i}(3)$ 。然后, 通过节点位移 $\delta_i = [u_i, v_i, w_i, \phi_i, \psi_i]^T$ 和形状函数 $N_i(s, t)$ 可以得到元素中任意一点的位移, 如下所示:

$$\begin{Bmatrix} u \\ v \\ w \end{Bmatrix} = \sum_{i=1}^8 N_i \begin{Bmatrix} u_i \\ v_i \\ w_i \end{Bmatrix} + \sum_{i=1}^8 \frac{n N_i t_i}{2} \begin{Bmatrix} l_{1i} & l_{2i} \\ m_{1i} & m_{2i} \\ n_{1i} & n_{2i} \end{Bmatrix} \begin{Bmatrix} \phi_i \\ \psi_i \end{Bmatrix} \quad (15)$$

然后, 矩阵 \mathbf{N} 由公式 15 定义为

$$\mathbf{N} = \begin{bmatrix} N_1 & 0 & 0 & \frac{n N_1 t_1}{2} l_{11} & \frac{n N_1 t_1}{2} l_{21} & \cdots \\ 0 & N_1 & 0 & \frac{n N_1 t_1}{2} m_{11} & \frac{n N_1 t_1}{2} m_{21} & \cdots \\ 0 & 0 & N_1 & \frac{n N_1 t_1}{2} n_{11} & \frac{n N_1 t_1}{2} n_{21} & \cdots \\ N_8 & 0 & 0 & \frac{n N_8 t_8}{2} l_{18} & \frac{n N_8 t_8}{2} l_{28} & \cdots \\ 0 & N_8 & 0 & \frac{n N_8 t_8}{2} m_{18} & \frac{n N_8 t_8}{2} m_{28} & \cdots \\ 0 & 0 & N_8 & \frac{n N_8 t_8}{2} n_{18} & \frac{n N_8 t_8}{2} n_{28} & \cdots \end{bmatrix} \quad (16)$$

定义几何矩阵 \mathbf{B} 为了获得局部坐标系中壳元素的应变, 局部坐标系的

应构建 $\mathbf{x}' - \mathbf{y}' - \mathbf{z}'$ 坐标系。 \mathbf{z}' 轴的构造如下

$$\mathbf{z}' = N_1 \mathbf{H}_{31} + N_2 \mathbf{H}_{32} + \cdots + N_8 \mathbf{H}_{38} \quad (17)$$

之后, 可以得到 \mathbf{z}' 的方向余弦 l_3, m_3, n_3 。然后, \mathbf{y}' 和 \mathbf{x}' 的构造为

$$\mathbf{y}' = \mathbf{z}' \times \mathbf{x} = \begin{bmatrix} i & j & k \\ l_3 & m_3 & n_3 \\ 1 & 0 & 0 \end{bmatrix}, \quad \mathbf{x}' = \mathbf{z}' \times \mathbf{y}' \quad (18)$$

可以得到 \mathbf{y}' 的方向余弦 l_2, m_2, n_2 和 \mathbf{x}' 的方向余弦 l_1, m_1, n_1 。然后, 局部坐标系 $\mathbf{x}' - \mathbf{y}' - \mathbf{z}'$ 的方向余弦矩阵可表示为

$$\mathbf{DCM} = \begin{bmatrix} l_1 & l_2 & l_3 \\ m_1 & m_2 & m_3 \\ n_1 & n_2 & n_3 \end{bmatrix} \quad (19)$$

矩阵 \mathbf{DCM} 用于将位移 u, v 和 w 的导数转换为局部位移 u', v' 和 w' 的导数。

$$\begin{bmatrix} \frac{\partial u'}{\partial x'} & \frac{\partial v'}{\partial x'} & \frac{\partial w'}{\partial x'} \\ \frac{\partial u'}{\partial y'} & \frac{\partial v'}{\partial y'} & \frac{\partial w'}{\partial y'} \\ \frac{\partial u'}{\partial z'} & \frac{\partial v'}{\partial z'} & \frac{\partial w'}{\partial z'} \end{bmatrix} = \mathbf{DCM}^T \begin{bmatrix} \frac{\partial u}{\partial x} & \frac{\partial v}{\partial x} & \frac{\partial w}{\partial x} \\ \frac{\partial u}{\partial y} & \frac{\partial v}{\partial y} & \frac{\partial w}{\partial y} \\ \frac{\partial u}{\partial z} & \frac{\partial v}{\partial z} & \frac{\partial w}{\partial z} \end{bmatrix} \mathbf{DCM} \quad (20)$$

其中:

$$\begin{bmatrix} \frac{\partial u}{\partial x} & \frac{\partial v}{\partial x} & \frac{\partial w}{\partial x} \\ \frac{\partial u}{\partial y} & \frac{\partial v}{\partial y} & \frac{\partial w}{\partial y} \\ \frac{\partial u}{\partial z} & \frac{\partial v}{\partial z} & \frac{\partial w}{\partial z} \end{bmatrix} = \mathbf{J}^{-1} \begin{bmatrix} \frac{\partial u}{\partial s} & \frac{\partial v}{\partial s} & \frac{\partial w}{\partial s} \\ \frac{\partial u}{\partial t} & \frac{\partial v}{\partial t} & \frac{\partial w}{\partial t} \\ \frac{\partial u}{\partial n} & \frac{\partial v}{\partial n} & \frac{\partial w}{\partial n} \end{bmatrix} \quad (21)$$

where **J** is the Jacobian matrix:

$$\mathbf{J} = \begin{bmatrix} \frac{\partial x}{\partial s} & \frac{\partial y}{\partial s} & \frac{\partial z}{\partial s} \\ \frac{\partial x}{\partial t} & \frac{\partial y}{\partial t} & \frac{\partial z}{\partial t} \\ \frac{\partial x}{\partial n} & \frac{\partial y}{\partial n} & \frac{\partial z}{\partial n} \end{bmatrix} \quad (22)$$

According to Eqs. 15 and 20 and the strain–displacement equations, the strain in the local coordinate system can be given by:

$$\varepsilon' = \begin{Bmatrix} \varepsilon'_x \\ \varepsilon'_y \\ \gamma'_{xy} \\ \gamma'_{yz} \\ \gamma'_{zx} \end{Bmatrix} = \begin{Bmatrix} \frac{\partial u'}{\partial x'} \\ \frac{\partial v'}{\partial y'} \\ \frac{\partial u'}{\partial y'} + \frac{\partial v'}{\partial x'} \\ \frac{\partial w'}{\partial y'} + \frac{\partial v'}{\partial z'} \\ \frac{\partial w'}{\partial x'} + \frac{\partial u'}{\partial z'} \end{Bmatrix} = \mathbf{B}\delta = \sum_{i=1}^8 \mathbf{B}_i \delta_i \quad (23)$$

The geometric matrix **B_i** can be expressed as:

$$\mathbf{B}_i^T = \begin{bmatrix} l_1\alpha_1 & l_2\alpha_2 & l_1\alpha_2 + l_2\alpha_1 \\ m_1\alpha_1 & m_2\alpha_2 & m_1\alpha_2 + m_2\alpha_1 \\ n_1\alpha_1 & n_2\alpha_2 & n_1\alpha_2 + n_2\alpha_1 \\ \beta_1\gamma_1 & \beta_2\gamma_2 & \beta_1\gamma_2 + \beta_2\gamma_1 \\ \beta_1\lambda & \beta_2\lambda_2 & \beta_1\lambda_2 + \beta_2\lambda_1 \\ l_2\alpha_3 + l_3\alpha_2 & l_3\alpha_1 + l_1\alpha_3 \\ m_2\alpha_3 + m_3\alpha_2 & m_3\alpha_1 + m_1\alpha_3 \\ n_2\alpha_3 + n_3\alpha_2 & n_3\alpha_1 + n_1\alpha_3 \\ \beta_2\gamma_3 + \beta_3\gamma_2 & \beta_3\gamma_1 + \beta_1\gamma_3 \\ \beta_2\lambda_3 + \beta_3\lambda_2 & \beta_3\lambda_1 + \beta_1\lambda_3 \end{bmatrix} \quad (24)$$

where:

$$\begin{cases} \alpha_s = l_s \frac{\partial N_i}{\partial x} + m_s \frac{\partial N_i}{\partial y} + n_s \frac{\partial N_i}{\partial z} \\ \beta_s = \left(l_s \frac{\partial P_i}{\partial x} + m_s \frac{\partial P_i}{\partial y} + n_s \frac{\partial P_i}{\partial z} \right) \frac{t_i}{2} \\ \gamma_s = l_s l_{1i} + m_s m_{1i} + n_s n_{1i} \\ \lambda_s = l_s l_{2i} + m_s m_{2i} + n_s n_{2i} \end{cases} \quad (25)$$

where $P_i = N_i n$. And $\mathbf{B} = [\mathbf{B}_1 \ \mathbf{B}_2 \ \cdots \ \mathbf{B}_8]$.

Mass and stiffness matrices of the shell element When the matrices **B**, **J**, and **N** have been obtained, the stiffness and mass matrices of the shell element can be written as:

$$\begin{aligned} \mathbf{K}_n &= \int_{-1}^1 \int_{-1}^1 \int_{-1}^1 \mathbf{B}^T \mathbf{D} \mathbf{B} |\mathbf{J}| ds dt dn \\ \mathbf{M}_n &= \int_{-1}^1 \int_{-1}^1 \int_{-1}^1 \rho \mathbf{N}^T \mathbf{N} |\mathbf{J}| ds dt dn \end{aligned} \quad (26)$$

where ρ is the density of the workpiece, and **D** is the elastic matrix.

$$\mathbf{D} = \frac{E}{1-\mu^2} \begin{bmatrix} 1 & \mu & 0 & 0 & 0 \\ \mu & 1 & 0 & 0 & 0 \\ 0 & 0 & \frac{1-\mu}{2} & 0 & 0 \\ 0 & 0 & 0 & \frac{1-\mu}{2k} & 0 \\ 0 & 0 & 0 & 0 & \frac{1-\mu}{2k} \end{bmatrix} \quad (27)$$

where E is the Young's modulus and μ is the Poisson's ratio. The factor k is taken as 1.2 to consider the influence of the uneven distribution of shear stress. It is time-consuming when the direct integration is used to calculate the triple integral in Eq. 26. So, the two-point Gaussian quadrature rule is used to calculate the mass and stiffness matrices of the shell element. The Gaussian integration of Eq. 26 can be expressed as:

$$\begin{aligned} \mathbf{K}_n &= \sum_{i=1}^8 \mathbf{B}^T(s_i, t_i, n_i) \mathbf{D} \mathbf{B}(s_i, t_i, n_i) |\mathbf{J}(s_i, t_i, n_i)| W_i W_j W_k \\ \mathbf{M}_n &= \sum_{i=1}^8 \rho \mathbf{N}^T(s_i, t_i, n_i) \mathbf{N}(s_i, t_i, n_i) |\mathbf{J}(s_i, t_i, n_i)| W_i W_j W_k \end{aligned} \quad (28)$$

The Gauss integral points and the corresponding weight coefficients are shown in Table 1.

Assembling the element matrices For obtaining the mass and stiffness matrices of the blade structure, the matrices obtained by Eq. 28 should be transformed to the global coordinate system. The transformation matrix can be expressed as:

$$\mathbf{L} = \begin{bmatrix} \gamma_1 & 0 & 0 & 0 & 0 & 0 & 0 & 0 \\ 0 & \gamma_2 & 0 & 0 & 0 & 0 & 0 & 0 \\ 0 & 0 & \gamma_3 & 0 & 0 & 0 & 0 & 0 \\ 0 & 0 & 0 & \gamma_4 & 0 & 0 & 0 & 0 \\ 0 & 0 & 0 & 0 & \gamma_5 & 0 & 0 & 0 \\ 0 & 0 & 0 & 0 & 0 & \gamma_6 & 0 & 0 \\ 0 & 0 & 0 & 0 & 0 & 0 & \gamma_7 & 0 \\ 0 & 0 & 0 & 0 & 0 & 0 & 0 & \gamma_8 \end{bmatrix} \quad (29)$$

Table 1 Gauss integral points and weight coefficients

Point i	1	2	3	4	5	6	7	8
s_i	1	1	−1	−1	1	1	−1	−1
t_i	1	−1	1	−1	1	−1	1	−1
n_i	1	1	1	1	−1	−1	−1	−1
W_i	$\frac{\sqrt{3}}{3}$	$\frac{\sqrt{3}}{3}$	$\frac{\sqrt{3}}{3}$	$\frac{\sqrt{3}}{3}$	$\frac{\sqrt{3}}{3}$	$\frac{\sqrt{3}}{3}$	$\frac{\sqrt{3}}{3}$	$\frac{\sqrt{3}}{3}$

其中, J 为雅各布矩阵:

$$\mathbf{J} = \begin{bmatrix} \frac{\partial x}{\partial s} & \frac{\partial y}{\partial s} & \frac{\partial z}{\partial s} \\ \frac{\partial x}{\partial t} & \frac{\partial y}{\partial t} & \frac{\partial z}{\partial t} \\ \frac{\partial x}{\partial n} & \frac{\partial y}{\partial n} & \frac{\partial z}{\partial n} \end{bmatrix} \quad (22)$$

根据公式 15 和 20 以及应变–位移方程, 局部坐标系中的应变可由以下公式给出:

$$\varepsilon' = \begin{Bmatrix} \varepsilon'_x \\ \varepsilon'_y \\ \gamma'_{xy} \\ \gamma'_{yz} \\ \gamma'_{zx} \end{Bmatrix} = \begin{Bmatrix} \frac{\partial u'}{\partial x'} \\ \frac{\partial v'}{\partial y'} \\ \frac{\partial u'}{\partial y'} + \frac{\partial v'}{\partial x'} \\ \frac{\partial w'}{\partial y'} + \frac{\partial v'}{\partial z'} \\ \frac{\partial w'}{\partial x'} + \frac{\partial u'}{\partial z'} \end{Bmatrix} = \mathbf{B}\delta = \sum_{i=1}^8 \mathbf{B}_i \delta_i \quad (23)$$

几何矩阵 **B_i** 可表示为

$$\mathbf{B}_i^T = \begin{bmatrix} l_1\alpha_1 & l_2\alpha_2 & l_1\alpha_2 + l_2\alpha_1 \\ m_1\alpha_1 & m_2\alpha_2 & m_1\alpha_2 + m_2\alpha_1 \\ n_1\alpha_1 & n_2\alpha_2 & n_1\alpha_2 + n_2\alpha_1 \\ \beta_1\gamma_1 & \beta_2\gamma_2 & \beta_1\gamma_2 + \beta_2\gamma_1 \\ \beta_1\lambda & \beta_2\lambda_2 & \beta_1\lambda_2 + \beta_2\lambda_1 \\ l_2\alpha_3 + l_3\alpha_2 & l_3\alpha_1 + l_1\alpha_3 \\ m_2\alpha_3 + m_3\alpha_2 & m_3\alpha_1 + m_1\alpha_3 \\ n_2\alpha_3 + n_3\alpha_2 & n_3\alpha_1 + n_1\alpha_3 \\ \beta_2\gamma_3 + \beta_3\gamma_2 & \beta_3\gamma_1 + \beta_1\gamma_3 \\ \beta_2\lambda_3 + \beta_3\lambda_2 & \beta_3\lambda_1 + \beta_1\lambda_3 \end{bmatrix} \quad (24)$$

其中

$$\begin{cases} \alpha_s = l_s \frac{\partial N_i}{\partial x} + m_s \frac{\partial N_i}{\partial y} + n_s \frac{\partial N_i}{\partial z} \\ \beta_s = \left(l_s \frac{\partial P_i}{\partial x} + m_s \frac{\partial P_i}{\partial y} + n_s \frac{\partial P_i}{\partial z} \right) \frac{t_i}{2} \\ \gamma_s = l_s l_{1i} + m_s m_{1i} + n_s n_{1i} \\ \lambda_s = l_s l_{2i} + m_s m_{2i} + n_s n_{2i} \end{cases} \quad (25)$$

ere $P_i = N_i n$. And $\mathbf{B} = [\mathbf{B}_1 \ \mathbf{B}_2 \ \cdots \ \mathbf{B}_8]$.

壳元素的质量和刚度矩阵 在得到矩阵 B、J 和 N 后, 壳元素的刚度矩阵和质量矩阵可写为

$$\begin{aligned} \mathbf{K}_n &= \int_{-1}^1 \int_{-1}^1 \int_{-1}^1 \mathbf{B}^T \mathbf{D} \mathbf{B} |\mathbf{J}| ds dt dn \\ \mathbf{M}_n &= \int_{-1}^1 \int_{-1}^1 \int_{-1}^1 \rho \mathbf{N}^T \mathbf{N} |\mathbf{J}| ds dt dn \end{aligned} \quad (26)$$

其中, ρ 为工件密度, D 为弹性矩阵。

$$\mathbf{D} = \frac{E}{1-\mu^2} \begin{bmatrix} 1 & \mu & 0 & 0 & 0 \\ \mu & 1 & 0 & 0 & 0 \\ 0 & 0 & \frac{1-\mu}{2} & 0 & 0 \\ 0 & 0 & 0 & \frac{1-\mu}{2k} & 0 \\ 0 & 0 & 0 & 0 & \frac{1-\mu}{2k} \end{bmatrix} \quad (27)$$

其中, E 为杨氏模量, μ 为泊松比。考虑到剪应力分布不均的影响, 系数 k 取为 1.2。采用直接积分法计算式 26 中的三重积分非常耗时。因此, 采用两点高斯正交法则来计算壳元素的质量矩阵和刚度矩阵。公式 26 的高斯积分可表示为

$$\begin{aligned} \mathbf{K}_n &= \sum_{i=1}^8 \mathbf{B}^T(s_i, t_i, n_i) \mathbf{D} \mathbf{B}(s_i, t_i, n_i) |\mathbf{J}(s_i, t_i, n_i)| W_i W_j W_k \\ \mathbf{M}_n &= \sum_{i=1}^8 \rho \mathbf{N}^T(s_i, t_i, n_i) \mathbf{N}(s_i, t_i, n_i) |\mathbf{J}(s_i, t_i, n_i)| W_i W_j W_k \end{aligned} \quad (28)$$

高斯积分点和相应的权重系数如表 1 所示。

组合元素矩阵 为了得到叶片结构的质量和刚度矩阵, 应将公式 28 得到的矩阵转换到全局坐标系。转换矩阵可表示为

$$\mathbf{L} = \begin{bmatrix} \gamma_1 & 0 & 0 & 0 & 0 & 0 & 0 & 0 \\ 0 & \gamma_2 & 0 & 0 & 0 & 0 & 0 & 0 \\ 0 & 0 & \gamma_3 & 0 & 0 & 0 & 0 & 0 \\ 0 & 0 & 0 & \gamma_4 & 0 & 0 & 0 & 0 \\ 0 & 0 & 0 & 0 & \gamma_5 & 0 & 0 & 0 \\ 0 & 0 & 0 & 0 & 0 & \gamma_6 & 0 & 0 \\ 0 & 0 & 0 & 0 & 0 & 0 & \gamma_7 & 0 \\ 0 & 0 & 0 & 0 & 0 & 0 & 0 & \gamma_8 \end{bmatrix} \quad (29)$$

表 1 高斯积分点和权重系数

点 i	1	2	3	4	5	6	7	8
s_i	1	1	−1	−1	1	1	−1	−1
t_i	1	−1	1	−1	1	−1	1	−1
n_i	1	1	1	1	−1	−1	−1	−1
W_i	$\frac{\sqrt{3}}{3}$	$\frac{\sqrt{3}}{3}$	$\frac{\sqrt{3}}{3}$	$\frac{\sqrt{3}}{3}$	$\frac{\sqrt{3}}{3}$	$\frac{\sqrt{3}}{3}$	$\frac{\sqrt{3}}{3}$	$\frac{\sqrt{3}}{3}$

where γ_i ($i = 1, 2, \dots, 8$) can be written as:

$$\gamma_i = \begin{bmatrix} l_{1i} & m_{1i} & n_{1i} & 0 & 0 \\ l_{2i} & m_{2i} & n_{2i} & 0 & 0 \\ l_{3i} & m_{3i} & n_{3i} & 0 & 0 \\ 0 & 0 & 0 & l_{1i} & m_{1i} \\ 0 & 0 & 0 & l_{2i} & m_{2i} \end{bmatrix} \quad (30)$$

The stiffness and mass matrices of the shell element in the global coordinate system can be defined as:

$$\mathbf{K}_n^e = \mathbf{L}^T \mathbf{K}_n \mathbf{L}; \mathbf{M}_n^e = \mathbf{L}^T \mathbf{M}_n \mathbf{L} \quad (31)$$

Then, the global stiffness and mass matrices of the blade can be obtained by the direct stiffness method [27].

$$\mathbf{K} = \sum_{n=1}^{Ne} \mathbf{K}_n^e; \mathbf{M} = \sum_{n=1}^{Ne} \mathbf{M}_n^e \quad (32)$$

where, Ne is the number of the elements of the FEM model.

3 Convergence analysis

After the mass and stiffness matrices of the FEM model have been obtained, the natural frequencies and the mode shapes of the workpiece can be calculated by Eq. 3. However, the number of DOF of the FEM model affects the calculation speed of the characteristic equation. For reducing the number of DOF of the model on the premise of guaranteeing the calculation accuracy, a convergence analysis is performed. Meanwhile, the numbers of DOF of the model built by shells (MBBS) and the model built by 3D cubes (MBBC) [20] are compared when the calculated natural frequencies achieve convergence.

The dimensions of the blade studied in this paper are shown in Fig. 4a and the corresponding part is shown in Fig. 4b. In order to make the workpiece, thicknesses are different along the x-direction, the upper surface of the blade is set as a stationary surface, and a draft of 0.5° is performed on the concave and convex surfaces of the blade in the 3D modeling process. The workpiece material is titanium alloy with density of 4500 kg/m^3 , Young's modulus of 104 GPa, and Poisson's ratio of 0.305. As the base of the blade is clamped by a fixture during machining, only the blade profile is modeled in the FEM modeling process to reduce the number of DOF of the model.

Matlab (R2014a) is used to build the FEM model of the blade based on the shell elements. To facilitate the following experimental verification, one element is set in the thickness direction, and five elements are set in the y-direction. The convergence of the natural frequencies is studied by increasing the number of elements (NOE) in the x-direction from 6 to 9 as shown in Fig. 5. Abaqus (6.14) is used to calculate the natural frequencies when the 3D cube elements with type of C3D20R are used to model the

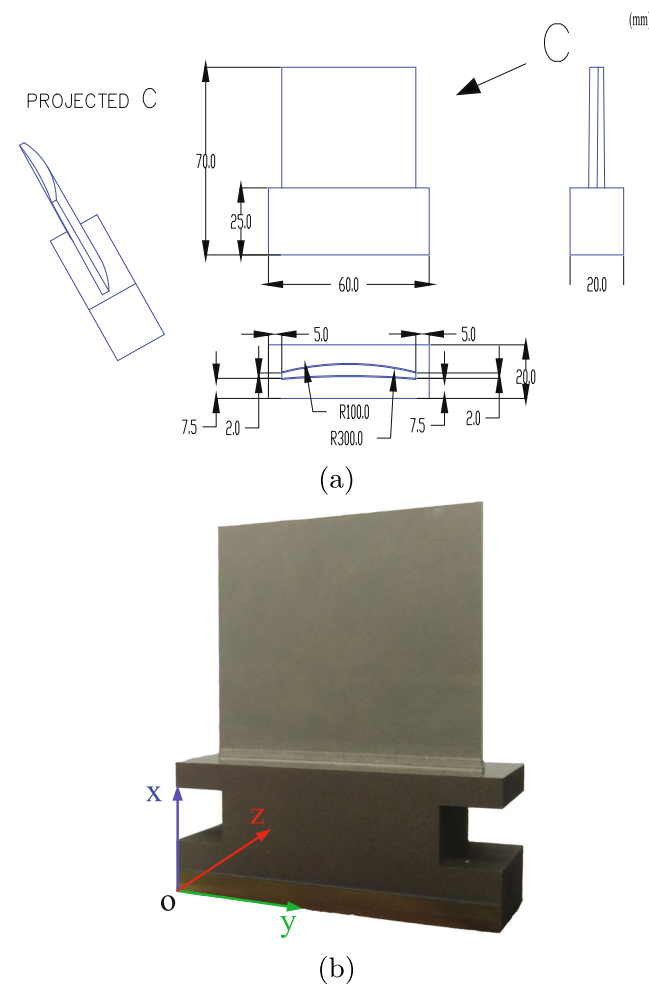


Fig. 4 a Dimensions of the blade structure and b blade part

blade. When the blade is meshed, two and five elements are set in the thickness direction and y-direction respectively. The convergence of the natural frequencies is studied by increasing the NOE in the x-direction from 4 to 8. As the high-order natural frequencies of the blade are difficult to be excited during machining, only the first four frequencies are studied in this paper. The convergence processes of the frequencies are shown in Fig. 6. The values in parentheses show the variations of the frequencies obtained by the present model and the previous model. Suppose that when the variations are less than 0.1%, the natural frequencies reach convergence.

As shown in Fig. 6a when the NOE increases from 35 to 40, the maximum variation of the first four natural frequencies is 0.053%. Therefore, when the numbers of shell elements in the y-direction and x-direction are 5 and 8 respectively, the calculated frequencies reach convergence. At this time, the number of DOF of the MBBS is 735, when the clamped-free boundary conditions (Fig. 5) are imposed on the model, the number of DOF is 680. Meanwhile, Fig. 6b

其中, γ_i ($i = 1, 2, \dots, 8$) 可写为

$$\gamma_i = \begin{bmatrix} l_{1i} & m_{1i} & n_{1i} & 0 & 0 \\ l_{2i} & m_{2i} & n_{2i} & 0 & 0 \\ l_{3i} & m_{3i} & n_{3i} & 0 & 0 \\ 0 & 0 & 0 & l_{1i} & m_{1i} \\ 0 & 0 & 0 & l_{2i} & m_{2i} \end{bmatrix} \quad (30)$$

全局坐标系中壳单元的刚度和质量矩阵可定义为

$$\mathbf{K}_n^e = \mathbf{L}^T \mathbf{K}_n \mathbf{L}; \mathbf{M}_n^e = \mathbf{L}^T \mathbf{M}_n \mathbf{L} \quad (31)$$

然后, 叶片的全局刚度和质量矩阵可通过直接刚度法求得 [27].

$$\mathbf{K} = \sum_{n=1}^{Ne} \mathbf{K}_n^e; \mathbf{M} = \sum_{n=1}^{Ne} \mathbf{M}_n^e \quad (32)$$

其中, Ne 是有限元模型的元素数。

3 收敛性分析

在得到有限元模型的质量和刚度矩阵后, 工件的固有频率和模态振型可通过公式 3 计算出来。然而, 有限元模型的 DOF 数会影响特征方程的计算速度。为了在保证计算精度的前提下减少模型的 DOF 数, 需要进行收敛分析。同时, 在计算固有频率达到收敛的情况下, 比较壳体 (MBBS) 模型和三维立方体 (MBBC) 模型的 DOF 数 [20]。

本文研究的叶片尺寸如图 4a 所示, 相应部分如图 4b 所示。为了制作工件, 沿 x 方向的厚度不同, 叶片上表面设为静止面, 并在三维建模过程中对叶片的凹面和凸面进行了 0.5° 的牵伸。工件材料为钛合金, 密度为 4500 kg/m^3 , 杨氏模量为 104 GPa, 泊松比为 0.305。由于叶片底部在加工过程中被夹具夹紧, 因此在有限元建模过程中只对叶片轮廓建模, 以减少模型的 DOF 数。

Matlab (R2014a) 用于建立基于壳元素的叶片有限元模型。为了便于接下来的实验验证, 在厚度方向上设置了一个元素, 在 y 方向上设置了五个元素。如图 5 所示, 通过将 x 方向的元素数 (NOE) 从 6 个增加到 9 个, 研究了自然频率的收敛性。当使用 C3D20R 类型的三维立方体元素建模时, 使用 Abaqus (6.14) 计算自然频率。

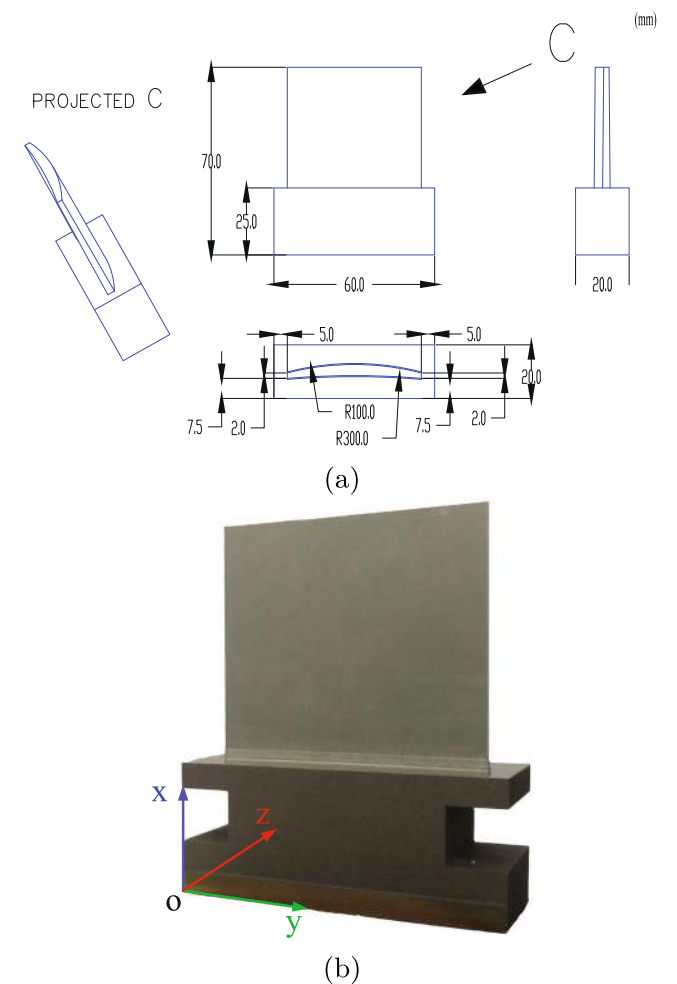


图 4 a 叶片结构尺寸和 b 叶片部分

叶片。对叶片进行网格划分时, 在厚度方向和 y 方向分别设置了两个和五个元素。通过将 x 方向上的 NOE 从 4 个增加到 8 个, 研究了自然频率的收敛性。由于叶片的高阶固有频率在加工过程中很难被激发, 因此本文只研究了前四个频率。频率的收敛过程如图 6 所示。括号中的数值表示本模型和前一模型得到的频率的变化。假设变化小于 0.1%, 则自然频率达到收敛。

如图 6a 所示, 当 NOE 从 35 增加到 40 时, 前四个自然频率的最大变化为 0.053%。因此, 当 y 方向和 x 方向的壳元素数量分别为 5 和 8 时, 计算出的频率达到收敛。此时 MBBS 的 DOF 数为 735, 当对模型施加无夹紧边界条件 (图 5) 时, DOF 数为 680。同时, 图 6b

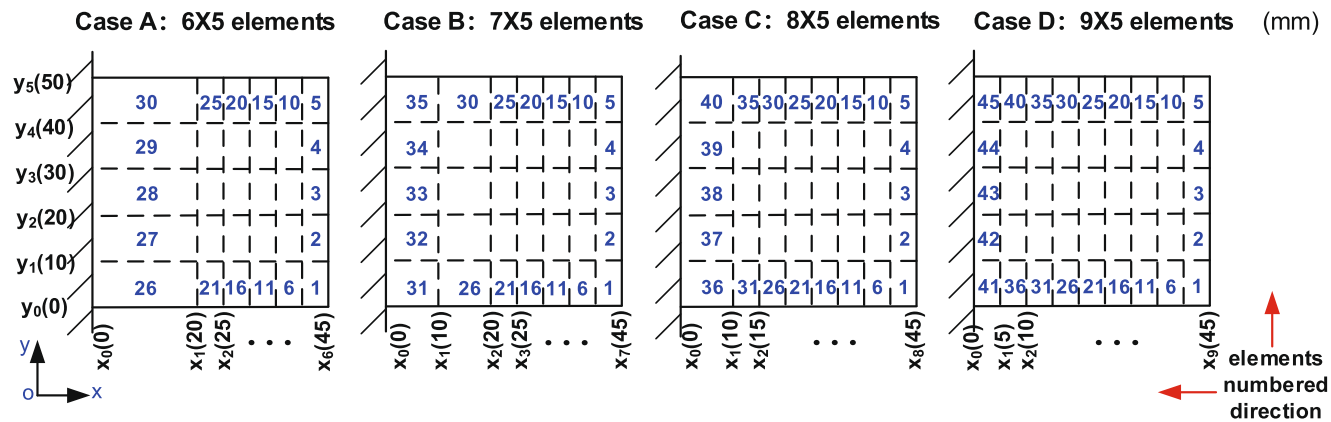


Fig. 5 Illustration of increasing the number of elements in the x-direction

shows that when the NOE increases from 60 to 70, the maximum variation is 0.075%. At this time, the number of DOF of the MBBC is 2916; when the clamped-free boundary conditions are applied, the number of DOF is 2646. One can see the number of DOF of the FEM model established by the 3D cube elements is 3.89 times the size of the model established by the shell elements. This leads to about 9 times faster computation of the eigenvalues when the shell elements are used. When the value obtained by the 3D cube elements is regarded as a standard, the maximum error of the first four frequencies calculated by the shell elements is 0.936% and the average error is 0.408%. Therefore, under the premise of guaranteeing the calculation accuracy, the shell elements can reduce the number of DOF of the FEM model and thus reduce the time of calculating the dynamics of the blade. In the following, the MBBS are used to calculate the workpiece dynamics. And one element is set in the thickness direction, five elements are set in the y-direction, and eight elements are set in the x-direction.

4 Prediction of time-variable workpiece dynamics

In order to select cutting parameters for avoiding resonance and chatter, the dynamics of the in-process workpiece (Fig. 7) must be known. In this section, a method based on Taylor series is proposed to predict the dynamics. The Taylor series in several variables can be expressed as:

$$f(x_1, x_2, \dots, x_n) = f(x_1^0, x_2^0, \dots, x_n^0) + \left(\Delta x_1 \frac{\partial f(x^0)}{\partial x_1} + \Delta x_2 \frac{\partial f(x^0)}{\partial x_2} + \dots + \Delta x_n \frac{\partial f(x^0)}{\partial x_n} \right) + \frac{1}{2!} \left(\Delta x_1 \frac{\partial}{\partial x_1} + \Delta x_2 \frac{\partial}{\partial x_2} + \dots + \Delta x_n \frac{\partial}{\partial x_n} \right)^2 f(x^0) + \frac{1}{3!} \left(\Delta x_1 \frac{\partial}{\partial x_1} + \Delta x_2 \frac{\partial}{\partial x_2} + \dots + \Delta x_n \frac{\partial}{\partial x_n} \right)^3 f(x^0) + \dots \quad (33)$$

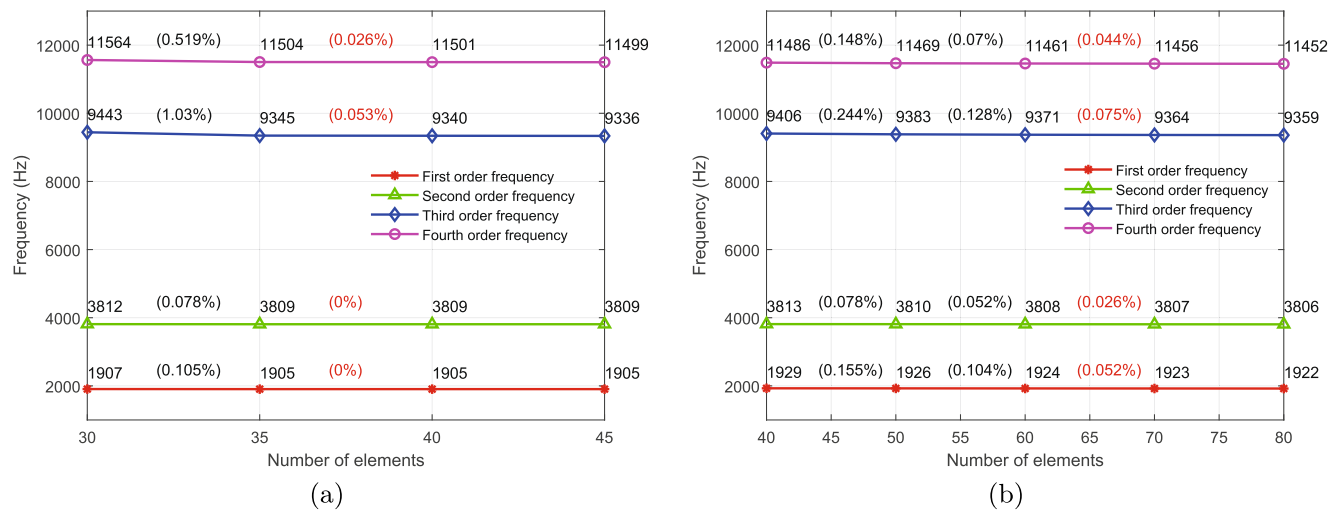


Fig. 6 Convergence process of the natural frequencies (Hz) **a** obtained by MBBS and **b** obtained by MBBC

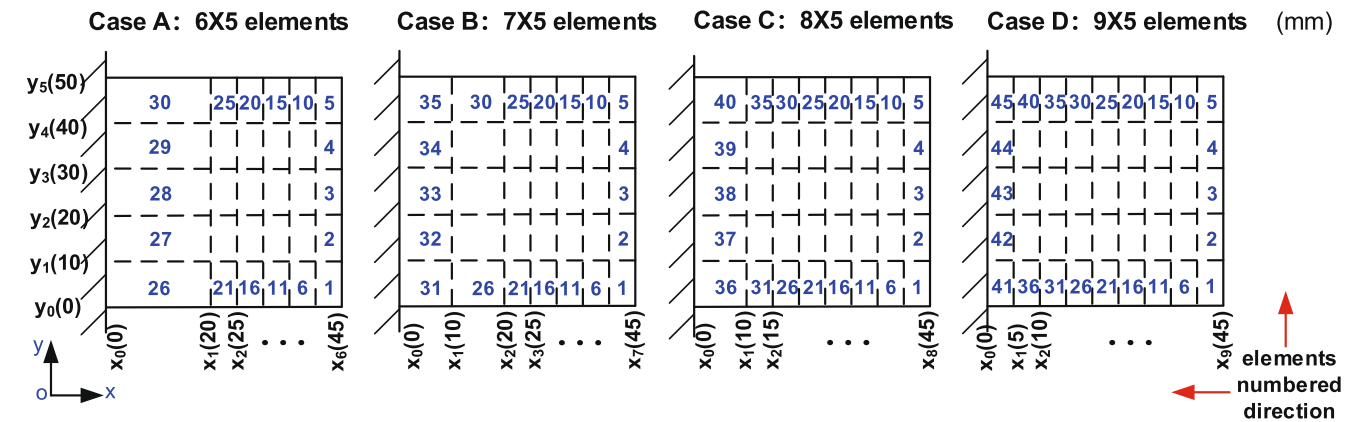


图 5 X 方向元素数量增加示意图

结果表明，当 NOE 从 60 增加到 70 时，最大变化为 0.075%。此时，MBBC 的 DOF 数为 2916；当应用无夹紧边界条件时，DOF 数为 2646。由此可见，由三维立方体元素建立的有限元模型的 DOF 数是由壳元素建立的模型的 3.89 倍。这使得使用壳元素计算特征值的速度提高了约 9 倍。如果以三维立方体元素得到的值为标准，壳元素计算的前四个频率的最大误差为 0.936%，平均误差为 0.408%。因此，在保证计算精度的前提下，壳元素可以减少有限元模型的 DOF 数，从而缩短叶片动力学计算的时间。下面采用 MBBS 计算工件动力学。在厚度方向上设置一个元素，在 y 方向上设置五个元素，在 x 方向上设置八个元素。

4 时变工件动力学预测

为了选择切削参数以避免共振和颤振，必须知道加工中工件的动态（图 7）。本节提出了一种基于泰勒级数的动态预测方法。多个变量的泰勒级数可表示为

$$f(x_1, x_2, \dots, x_n) = f(x_1^0, x_2^0, \dots, x_n^0) + \left(\Delta x_1 \frac{\partial f(x^0)}{\partial x_1} + \Delta x_2 \frac{\partial f(x^0)}{\partial x_2} + \dots + \Delta x_n \frac{\partial f(x^0)}{\partial x_n} \right) + \frac{1}{2!} \left(\Delta x_1 \frac{\partial}{\partial x_1} + \Delta x_2 \frac{\partial}{\partial x_2} + \dots + \Delta x_n \frac{\partial}{\partial x_n} \right)^2 f(x^0) + \frac{1}{3!} \left(\Delta x_1 \frac{\partial}{\partial x_1} + \Delta x_2 \frac{\partial}{\partial x_2} + \dots + \Delta x_n \frac{\partial}{\partial x_n} \right)^3 f(x^0) + \dots \quad (33)$$

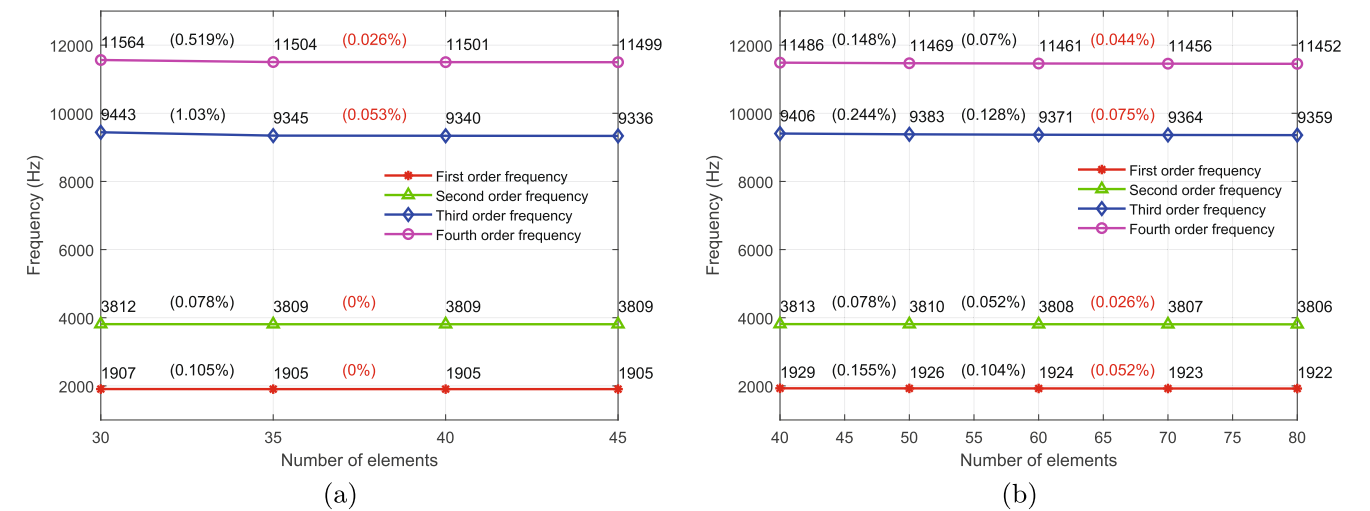


图 6 由 MBBS 和 MBBC 得出的自然频率（赫兹）**a** 和 **b** 的收敛过程

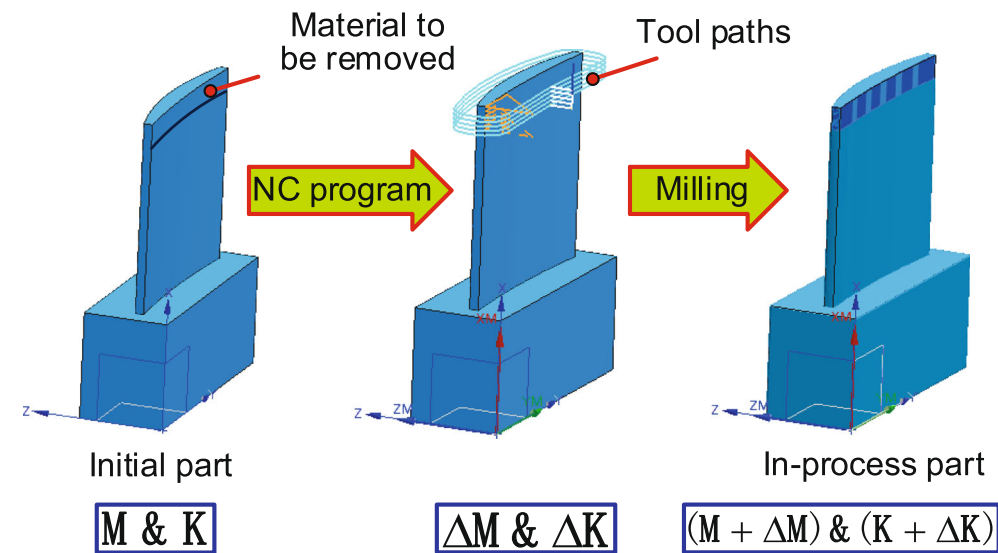


Fig. 7 Evolution procedure of workpiece dynamics

When the element mass matrix $\mathbf{M}_n(t^0)$ and stiffness matrix $\mathbf{K}_n(t^0)$ of the initial workpiece obtained by the MBBS are regarded as the functions of workpiece thickness, the variations $\Delta\mathbf{M}$, $\Delta\mathbf{K}$ caused by removed material can be obtained by Taylor series. Then, the mass and stiffness matrices $\mathbf{M}_n(t^1)$, $\mathbf{K}_n(t^1)$ of the in-process workpiece can be obtained by $\mathbf{M}_n(t^0) + \Delta\mathbf{M}$ and $\mathbf{K}_n(t^0) + \Delta\mathbf{K}$. By the calculation and comparison, a third-order Taylor series is used in this paper. The element stiffness matrix $\mathbf{K}_n(t^1)$ and mass matrix $\mathbf{M}_n(t^1)$ of the in-process workpiece can be expressed as:

$$\begin{aligned} \mathbf{K}_n(t^1) = & \mathbf{K}_n(t^0) + \sum_{i=1}^8 \Delta t_i \frac{\partial \mathbf{K}_n(t^0)}{\partial t_i} \\ & + \frac{1}{2!} \left(\Delta t_1 \frac{\partial}{\partial t_1} + \cdots + \Delta t_8 \frac{\partial}{\partial t_8} \right)^2 \mathbf{K}_n(t^0) \\ & + \frac{1}{3!} \left(\Delta t_1 \frac{\partial}{\partial t_1} + \cdots + \Delta t_8 \frac{\partial}{\partial t_8} \right)^3 \mathbf{K}_n(t^0) \end{aligned} \quad (34)$$

$$\begin{aligned} \mathbf{M}_n(t^1) = & \mathbf{M}_n(t^0) + \sum_{i=1}^8 \Delta t_i \frac{\partial \mathbf{M}_n(t^0)}{\partial t_i} \\ & + \frac{1}{2!} \left(\Delta t_1 \frac{\partial}{\partial t_1} + \cdots + \Delta t_8 \frac{\partial}{\partial t_8} \right)^2 \mathbf{M}_n(t^0) \\ & + \frac{1}{3!} \left(\Delta t_1 \frac{\partial}{\partial t_1} + \cdots + \Delta t_8 \frac{\partial}{\partial t_8} \right)^3 \mathbf{M}_n(t^0) \end{aligned} \quad (35)$$

where $t^0(t_1^0, \dots, t_i^0, \dots, t_8^0)$ and $t^1(t_1^1, \dots, t_i^1, \dots, t_8^1)$ are the thicknesses of the workpiece before and after machining, and Δt_i is the difference between t^1 and t^0 and its value is negative. The modeling process in Section 2.2 shows that the matrices \mathbf{B} , \mathbf{N} , and \mathbf{J} are the functions of t_i . Also, we

can get $\frac{\partial^2 \mathbf{B}}{\partial t_i^2} = 0$, $\frac{\partial^2 \mathbf{B}}{\partial t_i \partial t_{i+1}} = 0$, $\frac{\partial^2 \mathbf{N}}{\partial t_i^2} = 0$, $\frac{\partial^2 \mathbf{N}}{\partial t_i \partial t_{i+1}} = 0$, and $\frac{\partial^2 \mathbf{J}}{\partial t_i^2} = 0$. The detailed derivation of the partial derivatives of the matrices \mathbf{K}_n and \mathbf{M}_n with respect to thickness t_i is presented in Appendix A.

From the above equations, the process of computing $\mathbf{K}_n(t_i^1)$ and $\mathbf{M}_n(t_i^1)$ can be simplified to the calculation of $\frac{\partial \mathbf{J}}{\partial t_i}$, $\frac{\partial \mathbf{B}}{\partial t_i}$, and $\frac{\partial \mathbf{N}}{\partial t_i}$. And $\frac{\partial \mathbf{J}}{\partial t_i}$ can be obtained by Eq. 22, $\frac{\partial \mathbf{B}}{\partial t_i}$ can be obtained by Eqs. 24 and 25, and $\frac{\partial \mathbf{N}}{\partial t_i}$ can be obtained by Eq. 16. The variation Δt_i of workpiece thickness can be obtained by the radial depth of cut in milling. Then, the matrices $\mathbf{K}_n(t^1)$ and $\mathbf{M}_n(t^1)$ can be obtained by Eqs. 34 and 35, and the matrices in the global coordinate systems can be obtained by Eq. 31. And the stiffness matrix \mathbf{K}^1 and mass matrix \mathbf{M}^1 of the machined workpiece can be obtained by Eq. 32. After, the natural frequencies and the mode shapes of the blade can be obtained by Eq. 3.

5 Experimental validation and analysis

5.1 Modal testing

For verifying the accuracy of the method proposed in this paper, cutting and dynamic tests were performed on a machining center FVP-800A with a maximum spindle speed of 10,000 rpm, as shown in Fig. 8. The dimensions of the workpiece used in the tests are shown in Fig. 4, and the workpiece material is described in Section 3. In order to be consistent with the actual machining process of blade structures, a two-sided machining operation was adopted. A 4-flute end mill with 8 mm diameter was used in the experiments. The spindle speed, feed rate, and axial

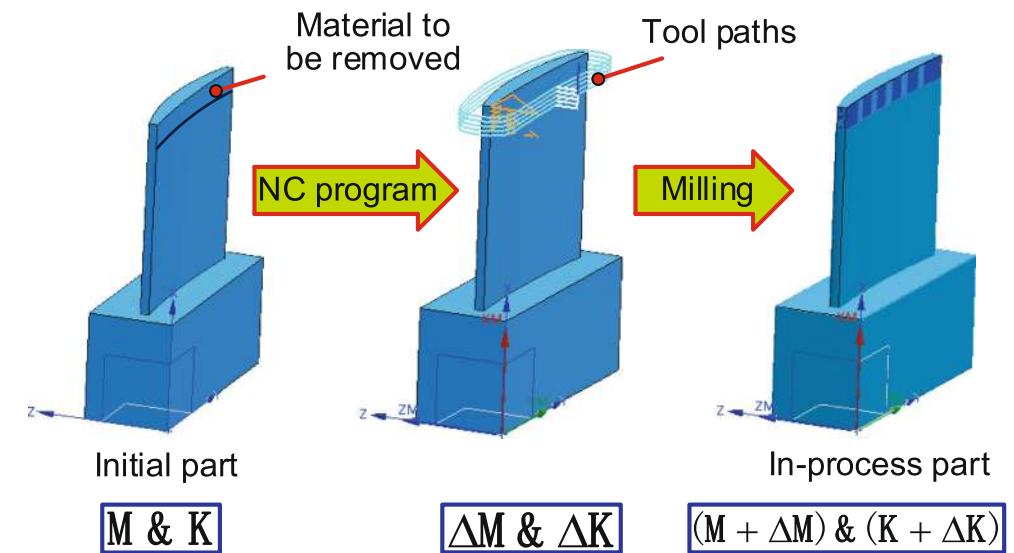


图 7 工件动力学演化过程

当将 MBBS 得到的初始工件的元素质量矩阵 $\mathbf{M}_n(t^0)$ 和刚度矩阵 $\mathbf{K}_n(t^0)$ 视为工件厚度的函数时，可通过泰勒级数求得去除材料引起的变化 $\Delta\mathbf{M}$, $\Delta\mathbf{K}$ 。然后，可通过 $\mathbf{M}_n(t^0) + \Delta\mathbf{M}$ 和 $\mathbf{K}_n(t^0) + \Delta\mathbf{K}$ 得到加工中工件的质量和刚度矩阵 $\mathbf{M}_n(t^1)$, $\mathbf{K}_n(t^1)$ 。通过计算和比较，本文采用了三阶泰勒级数。在制品工件的元素刚度矩阵 $\mathbf{K}_n(t^1)$ 和质量矩阵 $\mathbf{M}_n(t^1)$ 可表示为

$$\begin{aligned} \mathbf{K}_n(t^1) = & \mathbf{K}_n(t^0) + \sum_{i=1}^8 \Delta t_i \frac{\partial \mathbf{K}_n(t^0)}{\partial t_i} \\ & + \frac{1}{2!} \left(\Delta t_1 \frac{\partial}{\partial t_1} + \cdots + \Delta t_8 \frac{\partial}{\partial t_8} \right)^2 \mathbf{K}_n(t^0) \\ & + \frac{1}{3!} \left(\Delta t_1 \frac{\partial}{\partial t_1} + \cdots + \Delta t_8 \frac{\partial}{\partial t_8} \right)^3 \mathbf{K}_n(t^0) \end{aligned} \quad (34)$$

$$\begin{aligned} \mathbf{M}_n(t^1) = & \mathbf{M}_n(t^0) + \sum_{i=1}^8 \Delta t_i \frac{\partial \mathbf{M}_n(t^0)}{\partial t_i} \\ & + \frac{1}{2!} \left(\Delta t_1 \frac{\partial}{\partial t_1} + \cdots + \Delta t_8 \frac{\partial}{\partial t_8} \right)^2 \mathbf{M}_n(t^0) \\ & + \frac{1}{3!} \left(\Delta t_1 \frac{\partial}{\partial t_1} + \cdots + \Delta t_8 \frac{\partial}{\partial t_8} \right)^3 \mathbf{M}_n(t^0) \end{aligned} \quad (35)$$

其中， $t^0(t_1^0, \dots, t_i^0, \dots, t_8^0)$ 和 $t^1(t_1^1, \dots, t_i^1, \dots, t_8^1)$ 为加工前后的工件厚度， t_i 为 t^1 与 t^0 之差，其值为负。第 2.2 节中的建模过程表明，矩阵 \mathbf{B} 、 \mathbf{N} 和 \mathbf{J} 是 t_i 的函数。此外，我们

can get $\frac{\partial^2 \mathbf{B}}{\partial t_i^2} = 0$, $\frac{\partial^2 \mathbf{B}}{\partial t_i \partial t_{i+1}} = 0$, $\frac{\partial^2 \mathbf{N}}{\partial t_i^2} = 0$, $\frac{\partial^2 \mathbf{N}}{\partial t_i \partial t_{i+1}} = 0$, and $\frac{\partial^2 \mathbf{J}}{\partial t_i^2} = 0$. The detailed derivation of the partial derivatives of the matrices \mathbf{K}_n and \mathbf{M}_n with respect to thickness t_i is presented in Appendix A.

根据上述方程，计算 $\mathbf{K}_n(t^1)$ 和 $\mathbf{M}_n(t^1)$ 的过程可以简化为计算 $\frac{\partial \mathbf{J}}{\partial t_i}$, $\frac{\partial \mathbf{B}}{\partial t_i}$ 和 $\frac{\partial \mathbf{N}}{\partial t_i}$ 。由公式 22 得出， $\frac{\partial \mathbf{B}}{\partial t_i}$ 可由公式 24 和 25 得出， $\frac{\partial \mathbf{N}}{\partial t_i}$ 可由公式 16 得出。工件厚度的变化 t_i 可以通过铣削时的径向切削深度得到。然后，矩阵 $\mathbf{K}_n(t^1)$ 和 $\mathbf{M}_n(t^1)$ 可由式 34 和 35 求得，全局坐标系中的矩阵可由式 31 求得。加工工件的刚度矩阵 \mathbf{K}^1 和质量矩阵 \mathbf{M}^1 可由式 32 求得。之后，叶片的固有频率和模态振型可由式 3 得出。

5 实验验证和分析

5.1 模态测试

为验证本文所提方法的准确性，在主轴最高转速为 10,000 rpm 的加工中心 FVP-800A 上进行了切削和动态测试，如图 8 所示。测试所用工件的尺寸如图 4 所示，工件材料见第 3 节。为了与叶片结构的实际加工过程保持一致，采用了双面加工操作。实验中使用了直径为 8 毫米的 4 刃立铣刀。主轴转速、进给速度和轴向切削速度分别为

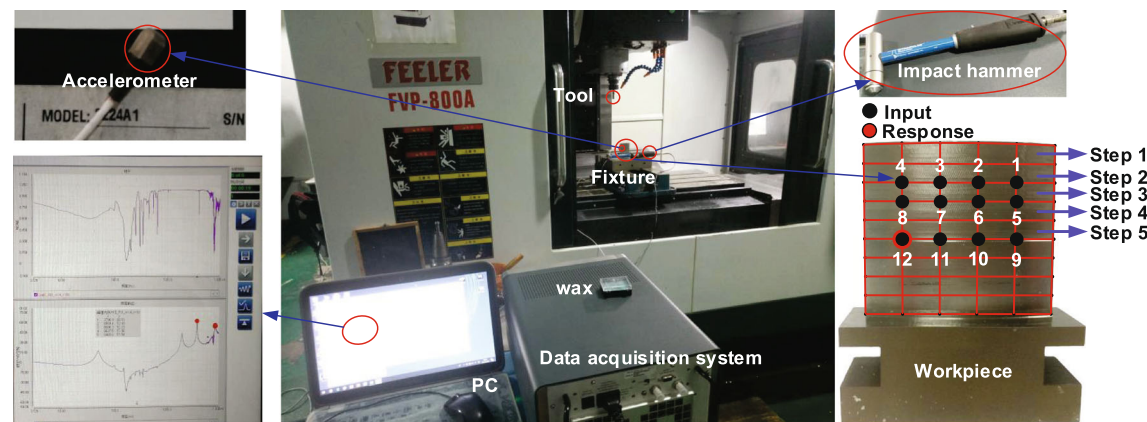


Fig. 8 Experimental setup and test spot

depth of cutting were 3000 rev/min, 300 mm/min, and 5 mm, respectively. And the radial depth of cut is $(0.2 + h * \tan(0.5))$, where h is the distance from the cutting point to the upper surface of the blade in the x-direction and 0.5 is the draft angle of the blade profile during 3D modeling.

Impact tests were carried out to obtain the dynamics of the blade at different machining steps. An impact hammer Dytran Model 5800B and an accelerometer Dytran 3224A1 were used in the tests. Due to the high natural frequencies of the workpiece studied in this paper, an aluminum alloy tip was selected so that the modes of interest can be excited. The data were acquired by the data acquisition system ECON-AVANT-8008 and processed by the modal analysis software supported by the Econ Corporation to extract the modal parameters of the workpiece. In order to ensure the reliability of tests and reduce the testing time, impact tests were performed for the workpiece at six cutting steps. Step 0 represents the initial state of the workpiece, and steps 1 to 5 represent the material has been removed with depths of 5 mm, 10 mm, 15 mm, 20 mm, and 25 mm, in x-direction.

Theoretically, there is no difference between roving hammer and roving accelerometer modal tests. However, the additional weight of the sensor affects the dynamics of the tested workpiece. When the accelerometer is attached to different positions of the workpiece, the obtained dynamics are different. Thus, in our tests, the accelerometer was fixed at a position and the hammer was moved around the workpiece. On the one hand, the accelerometer cannot be located at the mode nodes of the workpiece. On the other hand, the vibration amplitude of the accelerometer for the modes of interest should be obvious under the premise of reducing the influence of the additional weight on test results. According to the results of the FEM model, the positions of the accelerometer and impact points are shown in Fig. 8. Where point 12 is called the reference point since it is the response point for the all tests.

According to the characteristics of the blade, the impacts were applied along the z-direction at each impact point. Averaging techniques were used to reduce the effect of noise on the results. At each point, multiple impacts were performed and at least three sets of data with better coherence were selected for averaging. The FRFs of the workpiece, the coherence functions and the power spectrum of inputs were saved during tests. Then, the data were analyzed by the modal analysis software to obtain the dynamics of the blade.

5.2 Results analysis

5.2.1 Test results

The measured results of the initial workpiece are shown in Fig. 9; the FRF $H_{12,10}$ corresponds with applying the input at point 10 and measuring the response of point 12. It can be seen from Fig. 9a that the highest amplitude of the FRFs corresponds with mode 2. This is caused by the feature of the workpiece as shown in Fig. 4, since the dimension of the blade profile in the y-direction is larger than that in the x-direction, the torsional stiffness corresponding with mode 2 is weaker than the bending stiffness corresponding with mode 1. So, the torsional vibration is most likely to be excited during milling. Typically, the acceptability of the test results can be judged by the input power spectrum and the coherence functions. From Fig. 9b, one can see that the input power spectrum is flat over the range of the first frequency of the workpiece. And although there is a roll-off about 20 dB at mode 2, the coherence function is about 1. So, the workpiece dynamics of the first two modes obtained by the tests are acceptable. Meanwhile, past 5000 Hz, the input power spectrum has a significant roll-off, the coherence function is bad, and the FRF does not look good. Therefore, the error of the dynamics of mode 3 may be large. This results from the fact that there is not enough

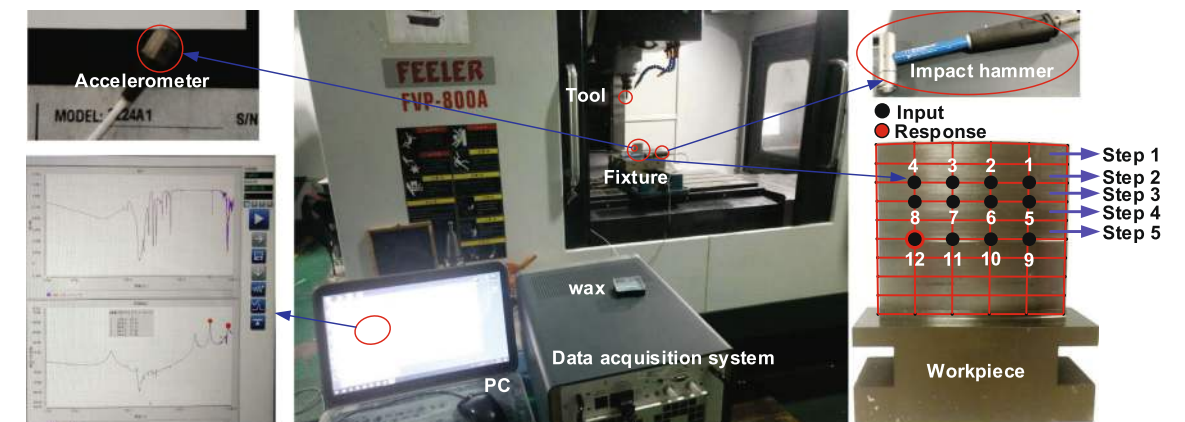


图 8 实验装置和测试点

切削深度分别为 3000 转/分钟、300 毫米/分钟和 5 毫米。径向切削深度为 $(0.2 + h * \tan(0.5))$ 其中, h 为切割点到刀片上表面在 x 方向上的距离, 0.5 为三维建模时刀片轮廓的拔模角度。

为了获得叶片在不同加工步骤下的动力学特性, 我们进行了冲击试验。测试中使用了 Dytran 5800B 型冲击锤和 Dytran 3224A1 型加速度计。由于本文研究的工件具有较高的固有频率, 因此选择了铝合金刀尖, 以便激发相关模式。数据由数据采集系统 ECON-AVANT-8008 采集, 并由 Econ 公司支持的模态分析软件进行处理, 以提取工件的模态参数。为了确保试验的可靠性并缩短试验时间, 对工件进行了六个切削步骤的冲击试验。第 0 步代表工件的初始状态, 第 1 至第 5 步代表材料已被移除, 在 x 方向上的深度分别为 5 毫米、10 毫米、15 毫米、20 毫米和 25 毫米。

从理论上讲, 巡回重锤和巡回加速度计模态测试没有区别。但是, 传感器的额外重量会影响被测工件的动态。当加速度计安装在工件的不同位置时, 获得的动态效果也不同。因此, 在我们的测试中, 加速度计固定在一个位置, 而锤子则围绕工件移动。一方面, 加速度计无法位于工件的模态节点处。另一方面, 在减少附加重量对测试结果影响的前提下, 加速度计对相关模态的振动幅度应该是明显的。根据有限元模型的结果, 加速度计和冲击点的位置如图 8 所示。其中第 12 点称为参考点, 因为它是所有测试的响应点。

根据叶片的特性, 在每个冲击点沿 Z 方向施加冲击。使用了平均技术来减少噪声对结果的影响。在每个点上都进行了多次冲击, 并选择了至少三组一致性较好的数据进行平均。测试期间保存了工件的 FRF、相干函数和输入功率谱。然后, 利用模态分析软件对数据进行分析, 以获得叶片的动力学特性。

5.2 结果分析

5.2.1 测试结果

初始工件的测量结果如图 9 所示; FRF $H_{12,10}$ 相当于在第 10 点输入并测量第 12 点的响应。从图 9a 可以看出, FRF 的最大振幅与模式 2 相对应。这是由于工件的特征造成的, 如图 4 所示, 由于叶片轮廓的 y 方向尺寸大于 x 方向尺寸, 与模式 2 相对应的扭转刚度弱于与模式 1 相对应的弯曲刚度。因此, 在铣削过程中最容易产生扭转振动。通常, 测试结果的可接受性可以通过输入功率谱和相干函数来判断。从图 9b 可以看出, 输入功率谱在工件的第一频率范围内是平坦的。因此, 测试得到的前两个模式的工件动态是可以接受的。同时, 超过 5000 Hz 时, 输入功率谱有明显的滚降, 相干函数不好, FRF 也不好看。因此, 模式 3 的动态误差可能较大。这是因为没有足够的

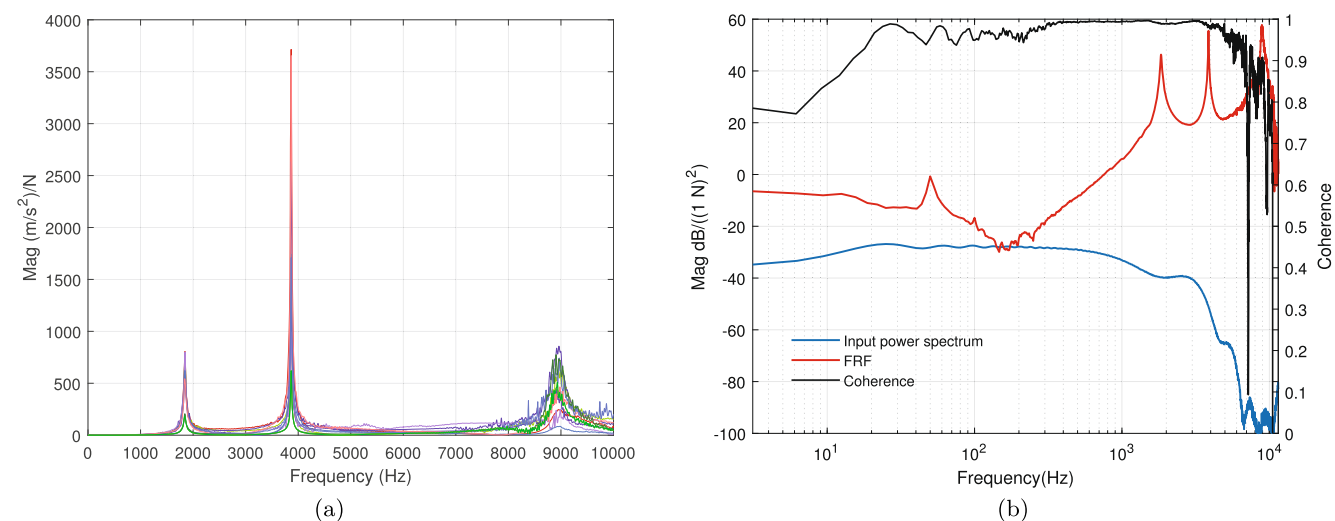


Fig. 9 Test results. **a** Amplitudes of the measured FRFs and **b** power spectrum of inputs and coherence corresponds with the FRF $H_{12,10}$

excitation at higher frequencies to cause the response of the workpiece.

The first three frequencies of the blade at different machining steps obtained by the tests are shown in Fig. 10. It can be seen that the material removal has a great influence on the workpiece dynamics. So, it is necessary to obtain the varying workpiece dynamics during milling for proper selection of machining parameters. In addition, the frequencies of modes 1 to 3 are different in the variation tendency. This shows that the material removal has different effects on the dynamics of modes 1 to 3.

5.2.2 Comparison

In order to use the FEM model of the initial workpiece to predict the workpiece dynamics in milling, the FRF $H_{12,10}$

obtained by the tests and the MBBS are compared, as shown in Fig. 11. It can be seen that over the range of the first two natural frequencies, the FRF obtained by the MBBS is in agreement with the test result. However, after 5000 Hz, the FRF obtained by the MBBS is inconsistent with the result obtained by the tests. This results from the modeling error of the FEM model and the measurement error of the tests. As the blade base was clamped by a fixture in milling, only the blade profile was modeled to reduce the number of DOF of the model. Then, the clamped-free boundary conditions were applied to the FEM model; there may be some differences between the applied boundary conditions and the actual situation. Meanwhile, the impact hammer cannot generate enough excitation at high frequency ranges to cause the response of the workpiece. So, at high frequency ranges, the waveform of the FRF curve is poor as shown in

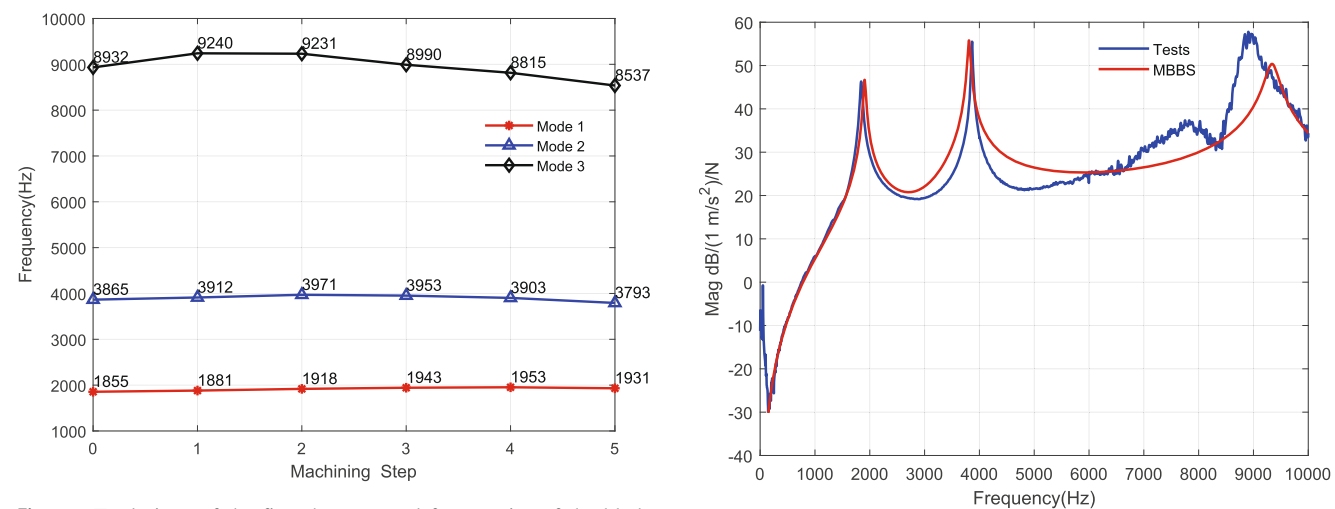


Fig. 10 Evolutions of the first three natural frequencies of the blade obtained by tests

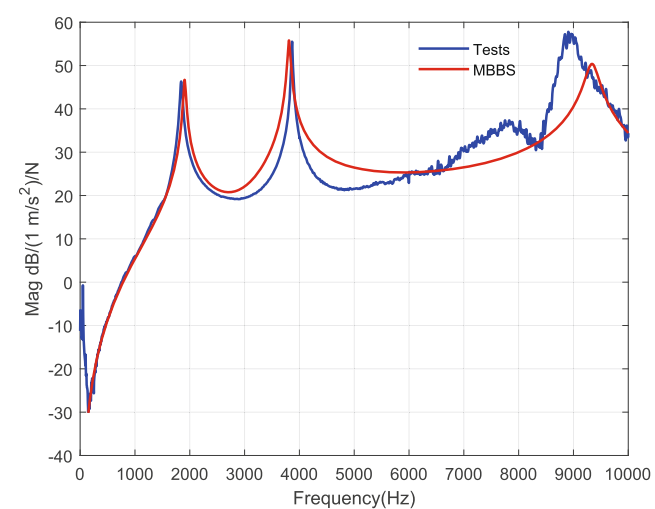


Fig. 11 Comparison of the FRF $H_{12,10}$ obtained by tests and MBBS

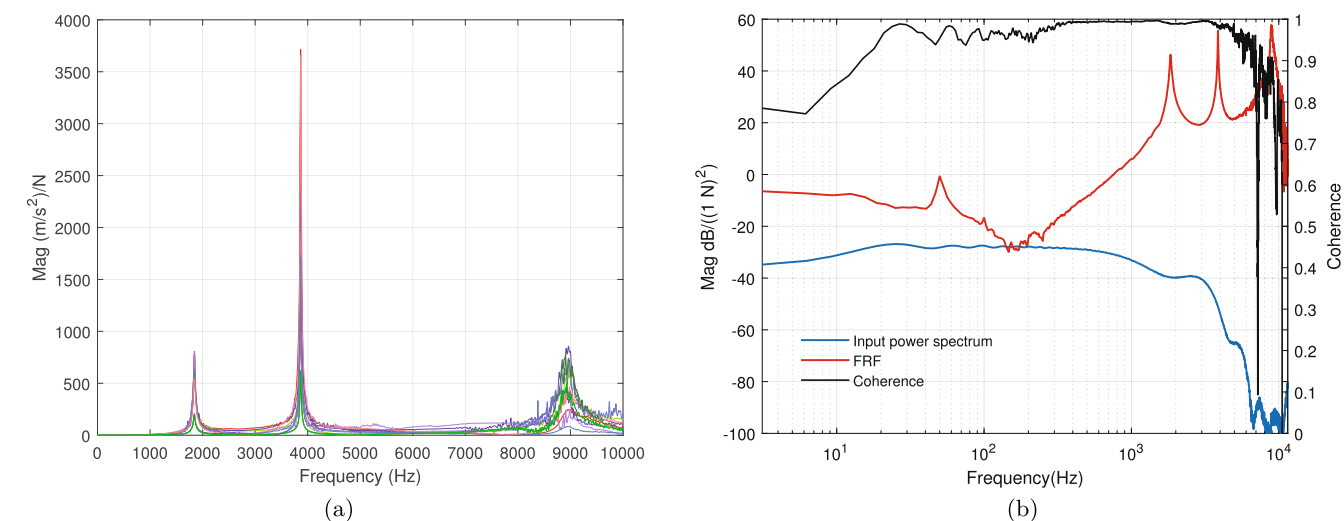


图 9 测试结果：a 测得的 FRF 的振幅和 b 输入和相干的功率谱对应于 FRF $H_{12,10}$

在较高频率下的激励会引起工件的响应。

试验得到的叶片在不同加工步骤下的前三个频率如图 10 所示。由此可见，材料去除量对工件动力学有很大影响。因此，有必要获取铣削过程中的工件动态变化，以正确选择加工参数。此外，模式 1 至 3 的频率变化趋势也不同。这表明材料去除对模式 1 至 3 的动态有不同的影响。

5.2.2 对比

为了利用初始工件的有限元模型来预测铣削过程中的工件动力学特性，将 FRF $H_{12,10}$

如图 11 所示，比较了测试和 MBBS 所获得的 FRF 值。可以看出，在前两个固有频率范围内，MBBS 得到的 FRF 与测试结果一致。然而，在 5000 Hz 之后，MBBS 得到的 FRF 与测试结果不一致。这是由于有限元模型的建模误差和测试的测量误差造成的。由于叶片底座在铣削过程中被夹具夹紧，为了减少模型的 DOF 数量，只对叶片轮廓进行了建模。然后，将无夹具边界条件应用于有限元模型；应用的边界条件与实际情况可能存在一些差异。同时，冲击锤在高频范围内无法产生足够的激励来引起工件的响应。因此，在高频范围内，FRF 曲线的波形较差，如图所示

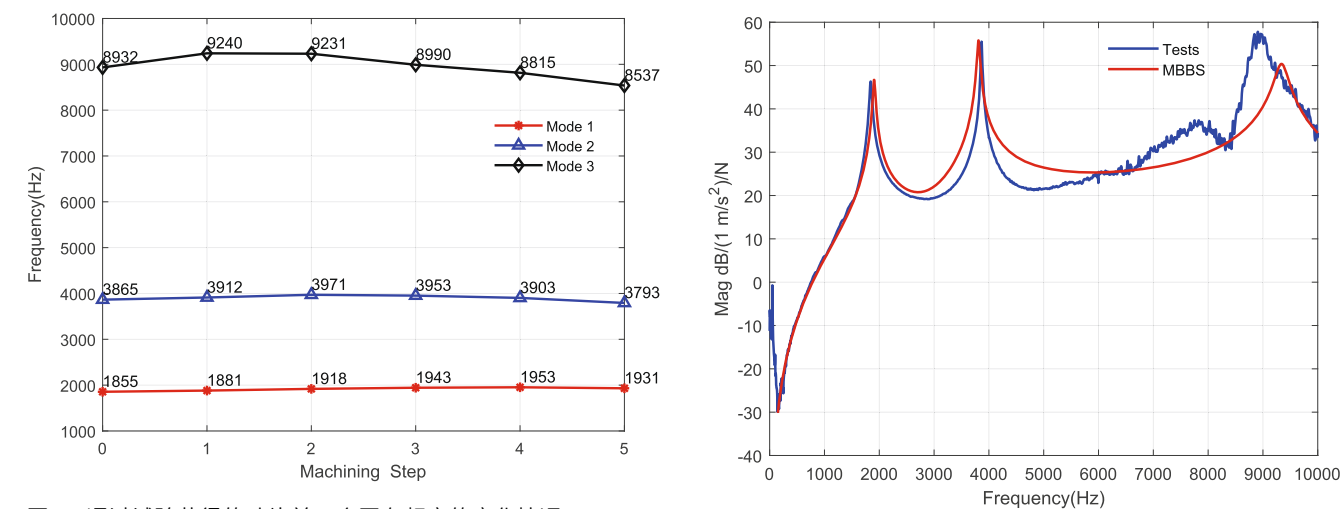


图 10 通过试验获得的叶片前三个固有频率的变化情况

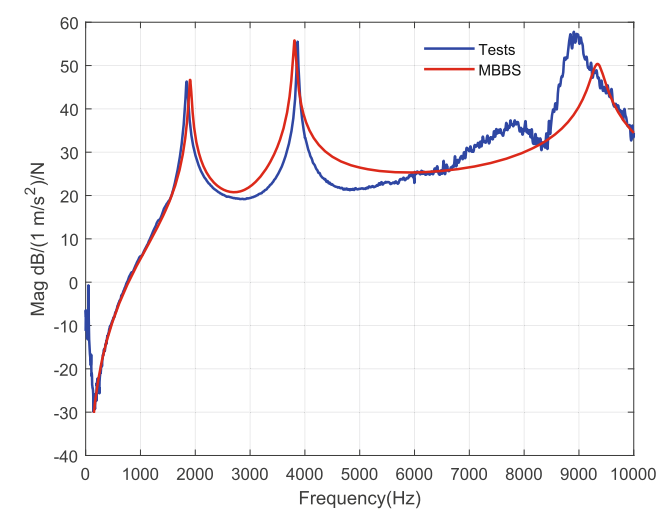


图 11 试验和 MBBS 所获 FRF $H_{12,10}$ 的比较

Fig. 9; therefore, the dynamics obtained by the tests may be deviated from the actual values. The mode shapes extracted from the RFRs obtained by the tests and the MBBS are compared as shown in Fig. 12, and the figures on the left show the results of the tests. It can be seen that the numerical values are consistent with the measured values, and the mode shapes of the modes 1 to 3 are 1st bending mode, 1st torsional mode, and 2nd bending mode, respectively.

Table 2 Comparison of the natural frequencies (Hz) of the initial workpiece obtained by tests and MBBS

Modes	1	2	3
Tests	1855	3865	8932
MBBS	1905	3809	9340
$\varepsilon(\%)$	(2.69)	(1.45)	(4.56)

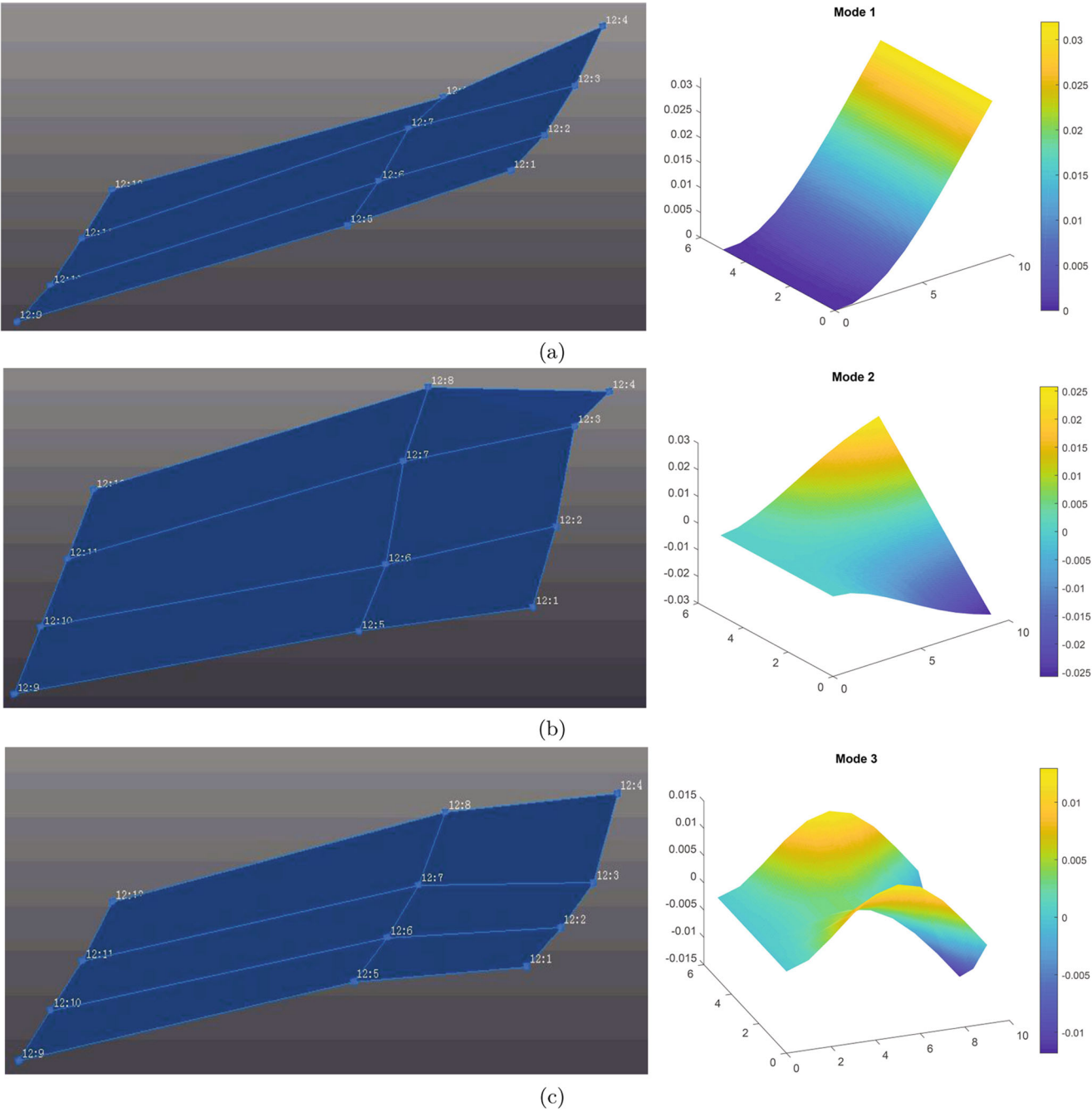


Fig. 12 Mode shapes obtained by tests and MBBS: **a** mode 1; **b** mode 2; and **c** mode 3

因此，试验获得的动力学值可能与实际值存在偏差。如图 12 所示，比较了测试和 MBBS 从 RFRs 中提取的模式振型。可以看出，数值与测量值一致，模式 1 至 3 的模式振型分别为第 1 弯曲模式、第 1 扭转模式和第 2 弯曲模式。

表 2 通过测试和 MBBS 获得的初始工件固有频率（赫兹）比较

模式	1	2	3
测试	1855	3865	8932
MBBS	1905	3809	9340
$\varepsilon(\%)$	(2.69)	(1.45)	(4.56)

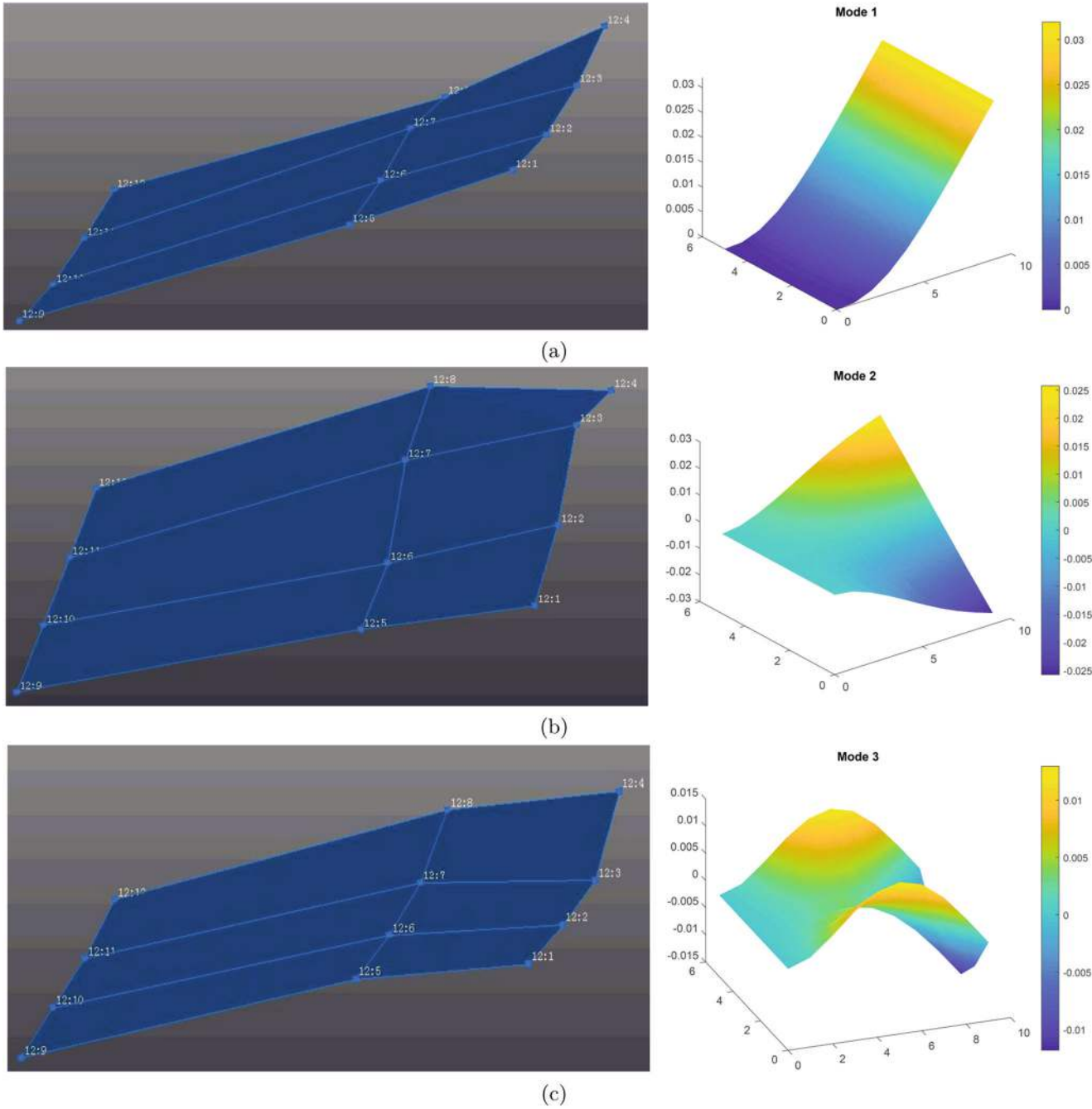


图 12 试验和 MBBS 得出的模式振型：a 模式 1；b 模式 2；c 模式 3

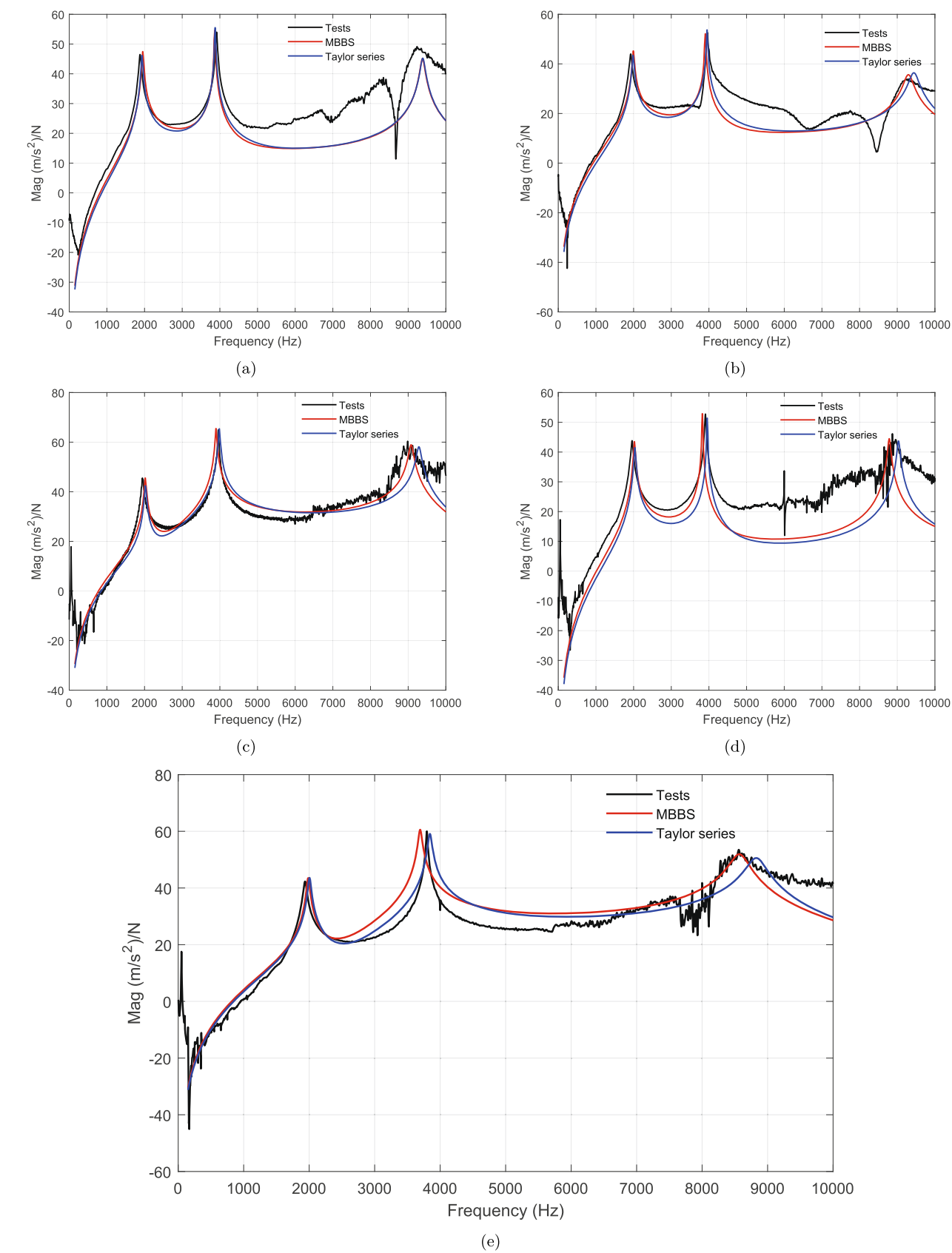


Fig. 13 Comparison of FRFs obtained by tests, MBBS, and Taylor series: **a** step 1 $H_{12,10}$; **b** step 2 $H_{12,9}$; **c** step 3 $H_{12,9}$; **d** step 4 $H_{12,10}$; and **e** step 5 $H_{12,9}$

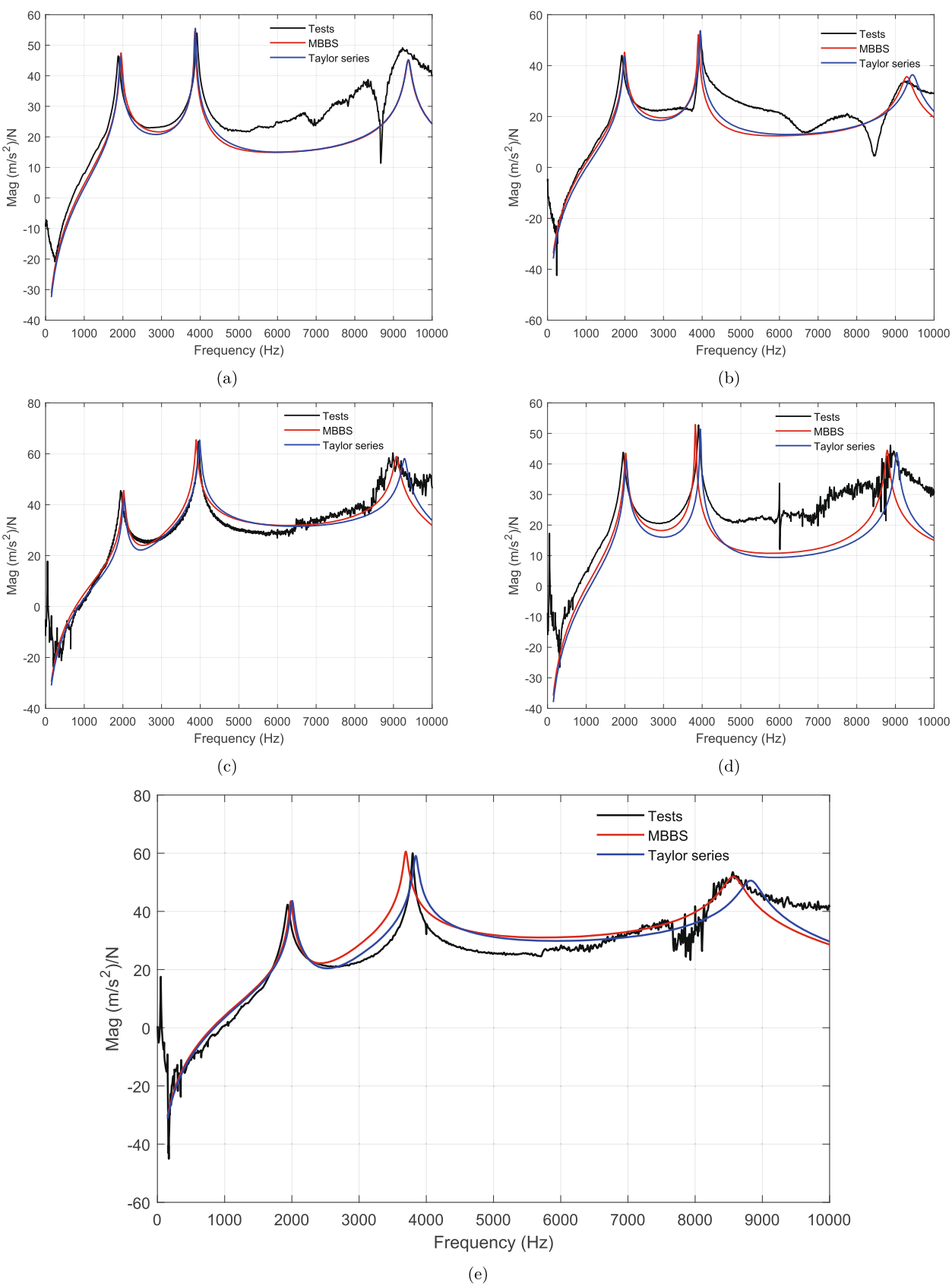


图 13 通过测试、MBBS 和泰勒级数获得的 FRF 比较: **a** 步骤 1 $H_{12,10}$; **b** 步骤 2 $H_{12,9}$; **c** 步骤 3 $H_{12,9}$; **d** 步骤 4 $H_{12,10}$; 和 **e** 步骤 5 $H_{12,9}$

Meanwhile, the natural frequencies obtained by the MBBS are compared with that obtained by the tests. The relative error is expressed as:

$$\varepsilon = \frac{|f_{Exp} - f_{MBBS}|}{f_{Exp}} \times 100\%$$

(36)

where f_{Exp} and f_{MBBS} are the frequencies obtained by the tests and the MBBS respectively. The results (Table 2) show that the maximum and average errors of the first three natural frequencies obtained by the MBBS are 4.56% and 2.9% respectively. Through the above analysis, it can be concluded that the MBBS can effectively calculate the dynamics of the initial workpiece.

Then, the varying workpiece dynamics in milling are predicted by the method proposed in Section 4 through the MBBS of the initial workpiece. The FRFs of the workpiece at different cutting steps obtained by the tests, the MBBS, and the Taylor series are compared in Fig. 13. It can seen that the FRFs obtained by the MBBS and the Taylor series can catch the FRFs obtained by the tests over the range of first two frequencies. In addition, the natural frequencies of the in-process workpiece obtained by the Taylor series and

the MBBC are compared with the values obtained by the tests. The relative errors are expressed as:

$$\eta_1 = \frac{|f_{MBBC} - f_{Exp}|}{f_{Exp}} \times 100\%$$

(37)

$$\eta_2 = \frac{|f_{Tay} - f_{Exp}|}{f_{Exp}} \times 100\%$$

(38)

where f_{MBBC} , f_{Exp} , and f_{Tay} are the frequencies obtained by the MBBC, the tests, and the Taylor series, respectively. The results are shown in Table 3, compared with the test results: the maximum and average errors of the frequencies at steps 1 to 5 obtained by the MBBC are 4.3% and 2.38%; 4.38% and 2.29%; 4.37% and 2.28%; 3.89% and 2.23%; 3.0% and 2.03%, respectively. Meanwhile, the maximum and average errors of the results obtained by the Taylor series are 2.53% and 1.67%; 3.44% and 2.07%; 4.06% and 2.83%; 4.04% and 2.70%; 3.83% and 2.83%, respectively.

From the above analysis, one can see that the proposed method can be used to accurately predict the dynamics of the blade in milling. When the volume of material removal is large, a higher order Taylor series or a MBBS of the workpiece at some machining steps can be used to improve the accuracy of prediction.

6 Conclusions

Workpiece dynamics is important for the stability of milling thin-walled parts. In this paper, a method based on the FEM model built by shell elements and a third-order Taylor series is proposed to calculate the dynamics of in-process workpieces during the machining of blade structures. In order to ensure the accuracy of the result and make the research more practical, the geometry of the blade structure is taken into consideration in the proposed method. The input data in the method is the mass and stiffness matrices of the initial workpiece which can be obtained by the FEM model, and the change of the matrices caused by material removal which can be obtained by the Taylor series. The convergence analysis of FEM models shows that, compared with the 3D cube elements, the shell elements can reduce the number of DOF of the FEM model by 74%, which leads to about 9 times faster computation of the eigenvalues. Meanwhile, the Taylor series can avoid frequently re-building and re-meshing the FEM model in the process of calculating workpiece dynamics. So, the efficiency of obtaining the workpiece dynamics can be improved by the proposed method. The result of impact tests shows that the FRFs obtained by the presented method can catch that obtained by the tests. And the maximum

同时, 将 MBBS 得出的自然频率与试验得出的自然频率进行比较。相对误差表示为

$$\varepsilon = \frac{|f_{Exp} - f_{MBBS}|}{f_{Exp}} \times 100\%$$

(36)

其中, f Exp 和 f MBBS 分别是测试和 MBBS 得到的频率。结果 (表 2) 显示, 通过 MBBS 获得的前三个自然频率的最大误差和平均误差分别为 4.56% 和 2.9%。通过以上分析, 可以得出结论: MBBS 可以有效地计算初始工件的动力学特性。

然后, 利用第 4 节中提出的方法, 通过初始工件的 MBBS 预测铣削过程中的工件动态变化。图 13 比较了试验、MBBS 和泰勒级数得到的不同切削步骤下的工件 FRF。从图中可以看出, 在前两个频率范围内, MBBS 和泰勒级数得到的 FRF 可以赶上测试得到的 FRF。此外, 泰勒级数和傅立叶变换得到的在制品工件的固有频率也与试验得到的固有频率一致。

表 3 通过测试、MBBC 和泰勒级数得到的不同加工步骤下刀片的固有频率 (赫兹)

加工步骤	模式	1	2	3
1	测试	1881	3912	9240
	MBBC	1962	3858	9375
	$\eta_1(\%)$	(4.3)	(1.38)	(1.46)
	泰勒系列	1930	3882	9400
	$\eta_2(\%)$	(2.53)	(0.767)	(1.73)
2	测试	1918	3971	9231
	MBBC	2002	3896	9288
	$\eta_1(\%)$	(4.38)	(1.88)	(0.617)
	泰勒序列	1984	3958	9458
	$\eta_2(\%)$	(3.44)	(0.327)	(2.46)
3	测试	1943	3953	8990
	MBBC	2028	3887	9062
	$\eta_1(\%)$	(4.37)	(1.67)	(0.8)
	泰勒系列	2022	3993	9299
	$\eta_2(\%)$	(4.06)	(1.01)	(3.43)
4	测试	1953	3903	8815
	MBBC	2029	3815	8766
	$\eta_1(\%)$	(3.89)	(2.25)	(0.55)
	泰勒系列	2032	3960	9045
	$\eta_2(\%)$	(4.04)	(1.46)	(2.61)
5	测试	1931	3793	8537
	MBBC	1989	3684	8557
	$\eta_1(\%)$	(3.0)	(2.87)	(0.23)
	泰勒系列	2005	3851	8841
	$\eta_2(\%)$	(3.83)	(1.53)	(3.12)

同时, 将 MBBS 得出的固有频率与试验得出的固有频率进行比较。相对误差表示为

$$\eta_1 = \frac{|f_{MBBC} - f_{Exp}|}{f_{Exp}} \times 100\%$$

(37)

$$\eta_2 = \frac{|f_{Tay} - f_{Exp}|}{f_{Exp}} \times 100\%$$

(38)

其中, f MBBC、f Exp 和 f Tay 分别为 MBBC、测试和泰勒级数得到的频率。结果如表 3 所示, 与测试结果相比: MBBC 得到的第 1 至 5 步频率的最大误差和平均误差分别为 4.3% 和 2.38%; 4.38% 和 2.29%; 4.37% 和 2.28%; 3.89% 和 2.23%; 3.0% 和 2.03%。同时, 泰勒级数所得结果的最大误差和平均误差分别为 2.53% 和 1.67%; 3.44% 和 2.07%; 4.06% 和 2.83%; 4.04% 和 2.70%; 3.83% 和 2.83%。

从以上分析可以看出, 所提出的方法可用于精确预测铣削过程中刀片的动力学特性。当材料去除量较大时, 可使用更高阶的泰勒级数或工件在某些加工步骤的 MBBS 来提高预测精度。

6 结论

工件动力学对于铣削薄壁零件的稳定性非常重要。本文提出了一种基于壳元素建立有限元模型和三阶泰勒级数的方法, 用于计算叶片结构加工过程中在制品的动力学特性。为了确保计算结果的准确性, 并使研究更具实用性, 所提出的方法考虑了叶片结构的几何形状。该方法的输入数据是初始工件的质量和刚度矩阵, 可通过有限元模型获得, 以及材料去除引起的矩阵变化, 可通过泰勒级数获得。有限元模型的收敛性分析表明, 与三维立方体元素相比, 壳元素可使有限元模型的 DOF 数减少 74%, 从而使特征值的计算速度提高约 9 倍。同时, 泰勒级数可以避免在计算工件动力学过程中频繁地重新建立有限元模型和重新网格划分。因此, 所提出的方法可以提高获取工件动力学信息的效率。冲击试验结果表明, 本文提出的方法所得到的 FRF 值与试验得到的 FRF 值相当。最大

error of the frequencies obtained by the proposed method is about 4%, which is approximately the same as the result obtained by the 3D cubes [26]. In addition, the limitation of measurement bandwidth caused by experimental conditions can be avoided by this method. For future study, the workpiece dynamics obtained by this method can be used to select cutting parameters for suppressing vibrations in the milling of blade structures.

Acknowledgements This work is supported by the National Natural Science Foundation of China (No. 51775444).

Appendix A: The partial derivatives of the matrices \mathbf{K}_n and \mathbf{M}_n

According to Eq. 26, the first-order partial derivatives of the matrices \mathbf{K}_n and \mathbf{M}_n with respect to thickness t_i can be described as:

$$\frac{\partial \mathbf{K}_n}{\partial t_i} = \iiint \left[\begin{array}{c} \frac{\partial \mathbf{B}^T}{\partial t_i} \mathbf{D} \mathbf{B} |\mathbf{J}| + \mathbf{B}^T \mathbf{D} \frac{\partial \mathbf{B}}{\partial t_i} |\mathbf{J}| \\ + \mathbf{B}^T \mathbf{D} \mathbf{B} \frac{\partial |\mathbf{J}|}{\partial t_i} \end{array} \right] ds dt dn \quad (\text{A.1})$$

$$\frac{\partial \mathbf{M}_n}{\partial t_i} = \rho \iiint \left[\begin{array}{c} \frac{\partial \mathbf{N}^T}{\partial t_i} \mathbf{N} |\mathbf{J}| + \mathbf{N}^T \frac{\partial \mathbf{N}}{\partial t_i} |\mathbf{J}| \\ + \mathbf{N}^T \mathbf{N} \frac{\partial |\mathbf{J}|}{\partial t_i} \end{array} \right] ds dt dn \quad (\text{A.2})$$

The second-order partial derivatives of the matrices \mathbf{K}_n and \mathbf{M}_n with respect to t_i can be described as:

$$\frac{\partial^2 \mathbf{K}}{\partial t_i^2} = \iiint \left[\begin{array}{c} 2 \frac{\partial \mathbf{B}^T}{\partial t_i} \mathbf{D} \frac{\partial \mathbf{B}}{\partial t_i} |\mathbf{J}| + 2 \frac{\partial \mathbf{B}^T}{\partial t_i} \mathbf{D} \mathbf{B} \frac{\partial |\mathbf{J}|}{\partial t_i} \\ + 2 \mathbf{B}^T \mathbf{D} \frac{\partial \mathbf{B}}{\partial t_i} \frac{\partial |\mathbf{J}|}{\partial t_i} + \mathbf{B}^T \mathbf{D} \mathbf{B} \frac{\partial^2 |\mathbf{J}|}{\partial t_i^2} \end{array} \right] ds dt dn \quad (\text{A.3})$$

$$\frac{\partial^2 \mathbf{M}}{\partial t_i^2} = \rho \iiint \left[\begin{array}{c} 2 \frac{\partial \mathbf{N}^T}{\partial t_i} \frac{\partial \mathbf{N}}{\partial t_i} |\mathbf{J}| + 2 \frac{\partial \mathbf{N}^T}{\partial t_i} \mathbf{N} \frac{\partial |\mathbf{J}|}{\partial t_i} \\ + 2 \mathbf{N}^T \frac{\partial \mathbf{N}}{\partial t_i} \frac{\partial |\mathbf{J}|}{\partial t_i} + \mathbf{N}^T \mathbf{N} \frac{\partial^2 |\mathbf{J}|}{\partial t_i^2} \end{array} \right] ds dt dn \quad (\text{A.4})$$

According to Eqs. A.1 and A.2, we can obtain:

$$\frac{\partial^2 \mathbf{K}_n}{\partial t_i \partial t_{i+1}} = \iiint \left[\begin{array}{c} \frac{\partial \mathbf{B}^T}{\partial t_i} \mathbf{D} \frac{\partial \mathbf{B}}{\partial t_{i+1}} |\mathbf{J}| \\ + \frac{\partial \mathbf{B}^T}{\partial t_i} \mathbf{D} \mathbf{B} \frac{\partial |\mathbf{J}|}{\partial t_{i+1}} \\ + \frac{\partial \mathbf{B}^T}{\partial t_{i+1}} \mathbf{D} \frac{\partial \mathbf{B}}{\partial t_i} |\mathbf{J}| \\ + \mathbf{B}^T \mathbf{D} \frac{\partial \mathbf{B}}{\partial t_i} \frac{\partial |\mathbf{J}|}{\partial t_{i+1}} \\ + \frac{\partial \mathbf{B}^T}{\partial t_{i+1}} \mathbf{D} \mathbf{B} \frac{\partial |\mathbf{J}|}{\partial t_i} \\ + \mathbf{B}^T \mathbf{D} \frac{\partial \mathbf{B}}{\partial t_{i+1}} \frac{\partial |\mathbf{J}|}{\partial t_i} \\ + \mathbf{B}^T \mathbf{D} \mathbf{B} \frac{\partial^2 |\mathbf{J}|}{\partial t_i \partial t_{i+1}} \end{array} \right] ds dt dn, \quad (i = 1, 2, \dots, 7) \quad (\text{A.5})$$

$$\frac{\partial^2 \mathbf{M}_n}{\partial t_i \partial t_{i+1}} = \rho \iiint \left[\begin{array}{c} \frac{\partial \mathbf{N}^T}{\partial t_i} \frac{\partial \mathbf{N}}{\partial t_{i+1}} |\mathbf{J}| \\ + \frac{\partial \mathbf{N}^T}{\partial t_i} \mathbf{N} \frac{\partial |\mathbf{J}|}{\partial t_{i+1}} \\ + \frac{\partial \mathbf{N}^T}{\partial t_{i+1}} \frac{\partial \mathbf{N}}{\partial t_i} |\mathbf{J}| \\ + \mathbf{N}^T \frac{\partial \mathbf{N}}{\partial t_i} \frac{\partial |\mathbf{J}|}{\partial t_{i+1}} \\ + \frac{\partial \mathbf{N}^T}{\partial t_{i+1}} \mathbf{N} \frac{\partial |\mathbf{J}|}{\partial t_i} \\ + \mathbf{N}^T \frac{\partial \mathbf{N}}{\partial t_{i+1}} \frac{\partial |\mathbf{J}|}{\partial t_i} \\ + \mathbf{N}^T \mathbf{N} \frac{\partial^2 |\mathbf{J}|}{\partial t_i \partial t_{i+1}} \end{array} \right] ds dt dn, \quad (i = 1, 2, \dots, 7) \quad (\text{A.6})$$

The first-order partial derivatives of the inverse matrix of the Jacobian matrix with respect to t_i can be expressed as:

$$\frac{\partial \mathbf{J}^{-1}}{\partial t_i} = -\mathbf{J}^{-1} \left(\frac{\partial \mathbf{J}}{\partial t_i} \right) \mathbf{J}^{-1} \quad (\text{A.7})$$

The first and second orders partial derivatives of the determinant $|\mathbf{J}|$ with respect to t_i can be expressed as:

$$\frac{\partial |\mathbf{J}|}{\partial t_i} = |\mathbf{J}| \text{Tr} \left(\mathbf{J}^{-1} \frac{\partial \mathbf{J}}{\partial t_i} \right) \quad (\text{A.8})$$

$$\frac{\partial^2 |\mathbf{J}|}{\partial t_i^2} = |\mathbf{J}| \left[\text{Tr} \left(\mathbf{J}^{-1} \frac{\partial \mathbf{J}}{\partial t_i} \right) \right]^2 + |\mathbf{J}| \text{Tr} \left[-\mathbf{J}^{-1} \left(\frac{\partial \mathbf{J}}{\partial t_i} \right) \mathbf{J}^{-1} \frac{\partial \mathbf{J}}{\partial t_i} \right] \quad (\text{A.9})$$

根据公式 A.1 和 A.2, 我们可以得出: 用拟议方法得到的频率误差约为 4%, 与三维立方体得到的结果大致相同 [26]。此外, 该方法还避免了实验条件对测量带宽的限制。在未来的研究中, 利用该方法获得的工件动力学参数可用于选择切削参数, 以抑制叶片结构铣削过程中的振动。

致谢 本研究得到了国家自然科学基金的资助 (编号: 51775444)。

附录 A: 矩阵 \mathbf{K}_n 和 \mathbf{M}_n 的偏导数

根据公式 26, 矩阵 \mathbf{K}_n 和 \mathbf{M}_n 关于厚度 t_i 的一阶偏导数可描述为:

$$\frac{\partial \mathbf{K}_n}{\partial t_i} = \iiint \left[\begin{array}{c} \frac{\partial \mathbf{B}^T}{\partial t_i} \mathbf{D} \mathbf{B} |\mathbf{J}| + \mathbf{B}^T \mathbf{D} \frac{\partial \mathbf{B}}{\partial t_i} |\mathbf{J}| \\ + \mathbf{B}^T \mathbf{D} \mathbf{B} \frac{\partial |\mathbf{J}|}{\partial t_i} \end{array} \right] ds dt dn \quad (\text{A.1})$$

$$\frac{\partial \mathbf{M}_n}{\partial t_i} = \rho \iiint \left[\begin{array}{c} \frac{\partial \mathbf{N}^T}{\partial t_i} \mathbf{N} |\mathbf{J}| + \mathbf{N}^T \frac{\partial \mathbf{N}}{\partial t_i} |\mathbf{J}| \\ + \mathbf{N}^T \mathbf{N} \frac{\partial |\mathbf{J}|}{\partial t_i} \end{array} \right] ds dt dn \quad (\text{A.2})$$

矩阵 \mathbf{K}_n 和 \mathbf{M}_n 关于厚度 t_i 的二阶偏导数可以描述为

$$\frac{\partial^2 \mathbf{K}}{\partial t_i^2} = \iiint \left[\begin{array}{c} 2 \frac{\partial \mathbf{B}^T}{\partial t_i} \mathbf{D} \frac{\partial \mathbf{B}}{\partial t_i} |\mathbf{J}| + 2 \frac{\partial \mathbf{B}^T}{\partial t_i} \mathbf{D} \mathbf{B} \frac{\partial |\mathbf{J}|}{\partial t_i} \\ + 2 \mathbf{B}^T \mathbf{D} \frac{\partial \mathbf{B}}{\partial t_i} \frac{\partial |\mathbf{J}|}{\partial t_i} + \mathbf{B}^T \mathbf{D} \mathbf{B} \frac{\partial^2 |\mathbf{J}|}{\partial t_i^2} \end{array} \right] ds dt dn$$

$$\frac{\partial^2 \mathbf{M}}{\partial t_i^2} = \rho \iiint \left[\begin{array}{c} 2 \frac{\partial \mathbf{N}^T}{\partial t_i} \frac{\partial \mathbf{N}}{\partial t_i} |\mathbf{J}| + 2 \frac{\partial \mathbf{N}^T}{\partial t_i} \mathbf{N} \frac{\partial |\mathbf{J}|}{\partial t_i} \\ + 2 \mathbf{N}^T \frac{\partial \mathbf{N}}{\partial t_i} \frac{\partial |\mathbf{J}|}{\partial t_i} + \mathbf{N}^T \mathbf{N} \frac{\partial^2 |\mathbf{J}|}{\partial t_i^2} \end{array} \right] ds dt dn$$

根据公式 A.1 和 A.2 我们可以得到

$$\frac{\partial^2 \mathbf{K}_n}{\partial t_i \partial t_{i+1}} = \iiint \left[\begin{array}{c} \frac{\partial \mathbf{B}^T}{\partial t_i} \mathbf{D} \frac{\partial \mathbf{B}}{\partial t_{i+1}} |\mathbf{J}| \\ + \frac{\partial \mathbf{B}^T}{\partial t_i} \mathbf{D} \mathbf{B} \frac{\partial |\mathbf{J}|}{\partial t_{i+1}} \\ + \frac{\partial \mathbf{B}^T}{\partial t_{i+1}} \mathbf{D} \frac{\partial \mathbf{B}}{\partial t_i} |\mathbf{J}| \\ + \mathbf{B}^T \mathbf{D} \frac{\partial \mathbf{B}}{\partial t_i} \frac{\partial |\mathbf{J}|}{\partial t_{i+1}} \\ + \frac{\partial \mathbf{B}^T}{\partial t_{i+1}} \mathbf{D} \mathbf{B} \frac{\partial |\mathbf{J}|}{\partial t_i} \\ + \mathbf{B}^T \mathbf{D} \frac{\partial \mathbf{B}}{\partial t_{i+1}} \frac{\partial |\mathbf{J}|}{\partial t_i} \\ + \mathbf{B}^T \mathbf{D} \mathbf{B} \frac{\partial^2 |\mathbf{J}|}{\partial t_i \partial t_{i+1}} \end{array} \right] ds dt dn, \quad (i = 1, 2, \dots, 7) \quad (\text{A.5})$$

$$\frac{\partial^2 \mathbf{M}_n}{\partial t_i \partial t_{i+1}} = \rho \iiint \left[\begin{array}{c} \frac{\partial \mathbf{N}^T}{\partial t_i} \frac{\partial \mathbf{N}}{\partial t_{i+1}} |\mathbf{J}| \\ + \frac{\partial \mathbf{N}^T}{\partial t_i} \mathbf{N} \frac{\partial |\mathbf{J}|}{\partial t_{i+1}} \\ + \frac{\partial \mathbf{N}^T}{\partial t_{i+1}} \frac{\partial \mathbf{N}}{\partial t_i} |\mathbf{J}| \\ + \mathbf{N}^T \frac{\partial \mathbf{N}}{\partial t_i} \frac{\partial |\mathbf{J}|}{\partial t_{i+1}} \\ + \frac{\partial \mathbf{N}^T}{\partial t_{i+1}} \mathbf{N} \frac{\partial |\mathbf{J}|}{\partial t_i} \\ + \mathbf{N}^T \frac{\partial \mathbf{N}}{\partial t_{i+1}} \frac{\partial |\mathbf{J}|}{\partial t_i} \\ + \mathbf{N}^T \mathbf{N} \frac{\partial^2 |\mathbf{J}|}{\partial t_i \partial t_{i+1}} \end{array} \right] ds dt dn, \quad (i = 1, 2, \dots, 7) \quad (\text{A.6})$$

雅各布矩阵的逆矩阵关于 t_i 的一阶偏导数可表示为

$$\frac{\partial \mathbf{J}^{-1}}{\partial t_i} = -\mathbf{J}^{-1} \left(\frac{\partial \mathbf{J}}{\partial t_i} \right) \mathbf{J}^{-1} \quad (\text{A.7})$$

行列式 $|\mathbf{J}|$ 关于 t_i 的一阶和二阶偏导数可表示为

$$\frac{\partial |\mathbf{J}|}{\partial t_i} = |\mathbf{J}| \text{Tr} \left(\mathbf{J}^{-1} \frac{\partial \mathbf{J}}{\partial t_i} \right) \quad (\text{A.8})$$

$$\frac{\partial^2 |\mathbf{J}|}{\partial t_i^2} = |\mathbf{J}| \left[\text{Tr} \left(\mathbf{J}^{-1} \frac{\partial \mathbf{J}}{\partial t_i} \right) \right]^2 + |\mathbf{J}| \text{Tr} \left[-\mathbf{J}^{-1} \left(\frac{\partial \mathbf{J}}{\partial t_i} \right) \mathbf{J}^{-1} \frac{\partial \mathbf{J}}{\partial t_i} \right] \quad (\text{A.9})$$

The second-order partial derivatives of the determinant $|\mathbf{J}|$ with respect to t_i and t_{i+1} can be expressed as:

$$\begin{aligned} \frac{\partial^2 |\mathbf{J}|}{\partial t_i \partial t_{i+1}} = & |\mathbf{J}| \operatorname{Tr} \left(\mathbf{J}^{-1} \frac{\partial \mathbf{J}}{\partial t_{i+1}} \right) \operatorname{Tr} \left(\mathbf{J}^{-1} \frac{\partial \mathbf{J}}{\partial t_i} \right) \\ & + |\mathbf{J}| \operatorname{Tr} \left[-\mathbf{J}^{-1} \left(\frac{\partial \mathbf{J}}{\partial t_{i+1}} \right) \mathbf{J}^{-1} \frac{\partial \mathbf{J}}{\partial t_i} \right], \end{aligned} \quad (i = 1, 2, \dots, 7) \tag{A.10}$$

In the above equations $i = 1, 2, \dots, 8$, when the value of i is not marked. Similarly, the third-order partial derivatives of the mass and stiffness matrices with respect to t_i can be obtained.

References

1. Tobias SA (1965) Machine-tool vibration. Blackie and Sons Ltd, New York

2. Smith S, Tlustý J (1993) Efficient simulation programs for chatter in milling. CIRP Ann Manuf Technol 42(1):463–466

3. Insperger T, Stépán G (2002) Semi-discretization method for delayed systems. Int J Numer Methods Eng 55(5):503–518

4. Ding Y, Zhu LM, Zhang XJ, Ding H (2010) A full-discretization method for prediction of milling stability. Int J Mach Tools Manuf 50(5):502–509

5. Bayly PV, Halley JE, Mann BP, Davies MA (2003) Stability of interrupted cutting by temporal finite element analysis. Trans ASME J Manuf Sci Eng 125(2):220–225

6. Altıntaş Y, Budak E (1995) Analytical prediction of stability lobes in milling. CIRP Ann Manuf Technol 44(1):357–362

7. Merdol SD, Altintas Y (2004) Multi frequency solution of chatter stability for low immersion milling. Trans ASME J Manuf Sci Eng 126(3):459–466

8. Yan BL, Zhu LD (2019) Research on milling stability of thin-walled parts based on improved multi-frequency solution. Int J Adv Manuf Technol 1–11

9. Comak A, Budak E (2017) Modeling dynamics and stability of variable pitch and helix milling tools for development of a design method to maximize chatter stability. Precis Eng 47:459–468

10. Bravo U, Altuzarra O, Lacalle De López LN, Sánchez JA, Campa FJ (2005) Stability limits of milling considering the flexibility of the workpiece and the machine. Int J Mach Tools Manuf 45(15):1669–1680

11. Seguy S, Campa FJ, Lacalle De López LN, Arnaud L, Dessein G, Aramendi G (2008) Toolpath dependent stability lobes for the milling of thin-walled parts. Int J Mach Machinabil Mater 4(4):377–392

12. Thévenot V, Arnaud L, Dessein G, Cazenave-Larroche G (2006) Influence of material removal on the dynamic behavior of

thin-walled structures in peripheral milling. Mach Sci Technol 10(3):275–287

13. Song QH, Ai X, Tang WX (2011) Prediction of simultaneous dynamic stability limit of time-variable parameters system in thin-walled workpiece high-speed milling processes. Int J Adv Manuf Technol 55(9-12):883–889

14. Crichigno Filho JM, Negri D, Melotti S (2018) Stable milling of cantilever plates using shell finite elements. Int J Adv Manuf Technol 99(9-12):2677–2693

15. Meshreki M, Attia H, Kövecses J (2011) Development of a new model for the varying dynamics of flexible pocket-structures during machining. J Manuf Sci Eng 133(4):041002

16. Song QH, Liu ZQ, Wan Y, Ju GG, Shi JH (2015) Application of sherman-morrison-woodbury formulas in instantaneous dynamic of peripheral milling for thin-walled component. Int J Mech Sci 96:79–90

17. Song QH, Shi JH, Liu ZQ, Wan Y (2017) A time-space discretization method in milling stability prediction of thin-walled component. Int J Adv Manuf Technol 89(9-12):2675–2689

18. Ahmadi K (2017) Finite strip modeling of the varying dynamics of thin-walled pocket structures during machining. Int J Adv Manuf Technol 89(9-12):2691–2699

19. Tuysuz O, Altintas Y (2017) Frequency domain updating of thin-walled workpiece dynamics using reduced order substructuring method in machining. J Manuf Sci Eng 139(7):071013

20. Yang Y, Zhang WH, Ma YC, Wan M (2016) Chatter prediction for the peripheral milling of thin-walled workpieces with curved surfaces. Int J Mach Tools Manuf 109:36–48

21. Tuysuz O, Altintas Y (2018) Time-domain modeling of varying dynamic characteristics in thin-wall machining using perturbation and reduced-order substructuring methods. J Manuf Sci Eng 140(1):011015

22. Dang XB, Wan M, Yang Y, Zhang WH (2019) Efficient prediction of varying dynamic characteristics in thin-wall milling using freedom and mode reduction methods. Int J Mech Sci 150:202–216

23. Luo M, Zhang DH, Wu BH, Tang M (2011) Modeling and analysis effects of material removal on machining dynamics in milling of thin-walled workpiece. Adv Mater Res 223:671–678. Trans Tech Publ

24. Tian WJ, Ren JX, Zhou JH, Wang DZ (2018) Dynamic modal prediction and experimental study of thin-walled workpiece removal based on perturbation method. Int J Adv Manuf Technol 94(5–8):2099–2113

25. Zienkiewicz OC, Taylor RL (2000) The finite element method: solid mechanics, vol 2. Butterworth-Heinemann, Oxford

26. Budak E, Tunç LT, Alan S, Özgüven HN (2012) Prediction of workpiece dynamics and its effects on chatter stability in milling. CIRP Ann Manuf Technol 61(1):339–342

27. Logan DL (2011) A first course in the finite element method. Cengage Learning, New York

Publisher’s note Springer Nature remains neutral with regard to jurisdictional claims in published maps and institutional affiliations.

行列式 $|\mathbf{J}|$ 关于 t_i 和 t_{i+1} 的二阶偏导数可表示为：

$$\begin{aligned} \frac{\partial^2 |\mathbf{J}|}{\partial t_i \partial t_{i+1}} = & |\mathbf{J}| \operatorname{Tr} \left(\mathbf{J}^{-1} \frac{\partial \mathbf{J}}{\partial t_{i+1}} \right) \operatorname{Tr} \left(\mathbf{J}^{-1} \frac{\partial \mathbf{J}}{\partial t_i} \right) \\ & + |\mathbf{J}| \operatorname{Tr} \left[-\mathbf{J}^{-1} \left(\frac{\partial \mathbf{J}}{\partial t_{i+1}} \right) \mathbf{J}^{-1} \frac{\partial \mathbf{J}}{\partial t_i} \right], \end{aligned} \quad (i = 1, 2, \dots, 7) \tag{A.10}$$

在上述公式中 $i = 1, 2, \dots, 8$ ，当 i 的值未标记时。同样，质量和刚度矩阵关于 t_i 的三阶偏导数也可求得。

参考文献

1.Tobias SA (1965) Machine-tool vibration.布莱克父子有限公司, 纽约 19.

2.Smith S, Tlustý J (1993) Efficient simulation programs for chatter in milling.CIRP Ann Manuf Technol 42(1):463–466

3.Insperger T, Stépán G (2002) Semi-discretization method for delayed systems.Int J Numer Methods Eng 55(5):503–518 4.

4.Ding Y, Zhu LM, Zhang XJ, Ding H (2010) A full-discretization method for prediction of milling stability.Int J Mach Tools Manuf 50(5):502–509 5.

5.Bayly PV, Halley JE, Mann BP, Davies MA (2003) Stability of interrupted cutting by temporal finite element analysis.Trans ASME J Manuf Sci Eng 125(2):220–225 22.

6.Altintas Y, Budak E (1995) Analytical prediction of stability lobes in milling.CIRP Ann Manuf Technol 44(1):357–362 7.

7.Merdol SD, Altintas Y (2004) 低浸入铣削颤振稳定性的多频率解决方案. Trans ASME J Manuf Sci Eng 126 (3) : 459–466 23.

8.Yan BL, Zhu LD (2019) 基于改进多频解法的薄壁零件铣削稳定性研究. Int J Adv Manuf Technol 1–11

9.Comak A, Budak E (2017) 对可变螺距和螺旋铣刀的动力学和稳定性进行建模，以开发最大化颤振稳定性的设计方法. Precis Eng 47:459–468 10.Bravo U, Altuzarra O, Lacalle De López LN, Sánchez JA, Campa FJ (2005) Stability limits of milling considering the flexibility of the workpiece and the machine.Int J Mach Tools Manuf 45(15):1669–1680

11.Seguy S, Campa FJ, Lacalle De López LN, Arnaud L, Dessein G, Aramendi G (2008) Toolpath dependent stability lobes for the milling of thin-walled parts.Int J Mach Machinabil Mater 4(4):377–392

12.Thévenot V, Arnaud L, Dessein G, Cazenave-Larroche G (2006) 《材料去除对材料动态行为的影响》。

外围铣削中的薄壁结构。机械科学与技术 10(3):275–287

13.Song QH, Ai X, Tang WX (2011) 薄壁工件高速铣削过程中时间可变参数系统的同步动态稳定极限预测. Int J Adv Manuf Technol 55(9–12):883–889

14.Crichigno Filho JM, Negri D, Melotti S (2018) 使用壳有限元对悬臂板进行稳定铣削. Int J Adv Manuf Technol 99(9–12):2677–2693

15.Meshreki M, Attia H, Kövecses J (2011) 为加工过程中柔性袋状结构的变化动力学开发新模型. J Manuf Sci Eng 133(4):041002 16.Song QH, Liu ZQ, Wan Y, Ju GG, Shi JH (2015) Sherman–morrison–woodbury 公式在薄壁零件外围铣削瞬时动力学中的应用. Int J Mech Sci 96:79–90

17.Song QH, Shi JH, Liu ZQ, Wan Y (2017) 一种时空离散化方法在薄壁构件铣削稳定性预测中的应用. Int J Adv Manuf Technol 89(9–12):2675–2689 18.Ahmadi K (2017) 加工过程中薄壁袋状结构变化动力学的有限条带建模. Int J Adv Manuf Technol 89(9–12):2691–2699

19.Tuysuz O, Altintas Y (2017) 在机械加工中使用减阶次结构法对薄壁工件动力学进行频域更新. J Manuf Sci Eng 139(7):071013 20.Yang Y, Zhang WH, Ma YC, Wan M (2016) 曲面薄壁工件外围铣削的颤振预测. Int J Mach Tools Manuf 109:36–48 21. Tuysuz O, Altintas Y (2018) 使用扰动和降阶次结构方法对薄壁加工中的变化动态特性进行时域建模. J Manuf Sci Eng 140(1):011015

22.Dang XB, Wan M, Yang Y, Zhang WH (2019) 使用自由度和模态还原方法高效预测薄壁铣削中的变化动态特性. Int J Mech Sci 150:202–216

23.Luo M, Zhang DH, Wu BH, Tang M (2011) 薄壁工件铣削中材料去除对加工动力学影响的建模与分析. Adv Mater Res 223:671–678. Trans Tech Publ

24.Tian WJ, Ren JX, Zhou JH, Wang DZ (2018) 基于扰动法的薄壁工件拆卸动态模态预测与实验研究. Int J Adv Manuf Technol 94(5–8):2099–2113

25.Zienkiewicz OC, Taylor RL (2000) The finite element method: solid mechanics, vol 2.Butterworth–Heinemann, Oxford 26.Budak E, Tunc LT, Alan S, Özgüven HN (2012) Prediction of workpiece dynamics and its effects on chatter stability in milling. CIRP Ann Manuf Technol 61(1):339–342 27.Logan DL (2011) A first course in the finite element method. Cengage Learning, 纽约

出版者注 Springer Nature 对出版地图和机构隶属关系中的管辖权主张保持中立。